Design and Analysis of a Non-Contact Tension Testing Device Based on Magnetic Levitation

MENGYI REN[ID]**, (Graduate Student Member, IEEE), AND KOICHI OKA**[ID]**, (Member, IEEE)**

Department of Intelligent Mechanical Systems Engineering, Kochi University of Technology, Kochi 7828502, Japan

Corresponding author: Koichi Oka (oka.koichi@kochi-tech.ac.jp)

ABSTRACT To facilitate mechanics testing in special environment, in this paper, a non-contact tension testing device was developed based on magnetic levitation technology. To find a floator that facilitates the alignment of tension force, electromagnetic analyses were performed using J-Mag software and a ring floator was found to be self-aligning. In addition, since the levitated objects need to bear a tension force, which will cause the nonlinearity of the magnetic levitation system to emerge, to address the nonlinear issue, a nonlinear mathematical model was established, and a centralized feedback linearization control algorithm was proposed. Furthermore, a tuning method for the control algorithm was proposed to deal with the mismatches between the controller and the plant. Moreover, a model for estimating specimen elongation was developed using support vector machine (SVM), the estimation results demonstrated that the range of the estimation error was between -0.1988mm and 0.2269mm, the root mean square error (RMSE) and coefficient of determination (R^2) were 0.0843mm and 98.76% respectively. Ultimately, a levitation experiment and a tension experiment were successfully performed, the levitation experiment results demonstrated that the proposed tuning method is effective and the centralized feedback linearization controller has stronger robustness to step disturbance than the traditional linear controller. The tension experiment results indicated that the whole control system copes well with an increasing tension force.

INDEX TERMS Magnetic levitation, tension testing device, structure optimization, feedback linearization, support vector machine.

I. INTRODUCTION

Generally, the process of traditional material mechanics testing is to apply some load to a specimen on a testing equipment, then remove the specimen from the testing equipment and observe it with imaging equipment, however, after the specimen is removed from the testing equipment, it is already in a different stress state to that during testing, so the observation results do not reflect the mechanics characteristics of the specimen when bearing the load [1]–[3]. A better alternative is in-situ testing, which is defined as observing a specimen while it is bearing some load. The imaging equipment suitable for in-situ observation includes scanning electron microscope (SEM), metalloscope and ultra-depth microscope, etc. Among these, SEM is being used more and more commonly in in-situ testing [4]–[7]. However, when using a SEM, the specimen needs to be placed in the vacuum chamber of the SEM. This means that for in-situ testing based on SEM, a

The associate editor coordinating the review of this manuscript and approving it for publication was Paolo Bettini.

load needs to be applied to the specimen inside the vacuum chamber of the SEM. Therefore, in-situ testing based on SEM was either done with a large vacuum chamber or with a small testing equipment. The former is costly, while the latter probably does not generate sufficient load forces. A more sensible approach is to apply a non-contact force from the outside of the vacuum chamber to the specimen inside the vacuum chamber. Magnetic levitation (maglev) technology makes this possible. In this paper, a maglev tension testing device (MLTTD), where the specimen can be pulled in a non-contact way, was developed. In addition to in-situ testing, MLTTD can also be used for mechanics testing of material in other special environments, such as testing the solder joints in corrosive, saline and humid environments, these testing was described in paper [8], [9].

Furthermore, another advantage of applying maglev technology to mechanics testing of material is that maglev technology can produce a much purer force as the levitation of an object is highly dependent on the balance of forces. Once a specimen is successfully tested in levitation, it will

not be mixed with any force in a direction other than the desired direction. Therefore, it probably allows higher testing accuracy. This makes sense for the mechanics testing of some micro materials [10]–[12].

Naoya, *et al.* [13], [14] at Okayama University developed a non-contact tension testing device where a permanent magnet was used to exert a non-contact tension force to the specimen. To control the amount of the tension force, the device employed a linear actuator to move the specimen close to or away from a permanent magnet. Furthermore, this device successfully tested the copper-cored lead-free solder ball and nickel rod joints in air, distilled water, and NaCl solution. However, only one end of the specimen was contactless while there was still contact at the other end of the specimen. In this case, the container in which the specimen is cannot be sealed, so it is impossible to perform testing in a vacuum chamber or other sealed environment. It may be a solution to fix one end of the specimen to the inner wall of the container and apply a non-contact force to the other end of the specimen, but this means that the container needs to bear the load force. Therefore, this method will not apply if the container is fragile or soft. As a better solution, MLTTD in this paper allows both ends of the specimen to be contactless with the container. Thus, it can be used in not only in-situ testing based on SEM but also the testing in other special environment.

To sum up the above, the development of a maglev mechanics testing device is significant for many applications. Apart from the application, this technique of destroying things through the air is novel and innovative in itself. It will probably play a role in other fields.

Moreover, it is necessary to consider control algorithms for MLTTD. Control algorithms for magnetic levitation have long been a hot topic of research. In recent years, various control algorithms [15]–[17] have been proposed for magnetic levitation. They are no more than PID control, sliding mode control, fuzzy control, robust control, fractional order control, neural network control, etc., and the combinations of these. Although many novel control algorithms have been proposed, traditional PID control keep dominant in industrial application. One reason is that many of the novel control algorithms are only based on theoretical studies and have not been experimentally validated. Another reason is that there is no standard tuning method for these novel control algorithms. Besides, to facilitate research, many studies on maglev control algorithms were conducted based on single-DoF maglev systems. In contrast, MLTTD is a 2-DoF maglev system. Therefore, these studies may not provide a valuable reference. For MLTTD, the most critical issue is maintaining levitation while the levitated object is bearing tension force. Traditional linear control algorithms, such as PD, PID, linear state feedback, are based on the linearization around a fixed equilibrium point where the magnetic force exactly counteracts the gravity of the levitated object. In applying tension force, the working point will inevitably deviate far from the original equilibrium point, so the traditional linear algorithms are not applicable. With the rise of artificial intelligence,

some intelligent algorithms have been proposed. Sun [18] designed an amplitude saturation controller for a maglev train, and this controller was proven to be robust to time delay after it was improved by a radial basis function neural network; also, based on deep learning, Sun proposed a semi-supervised controller [19], which can cope well with external disturbances within a bounded range of airgap. Wai [20] designed a backstepping fuzzy-neural-network controller for a hybrid maglev transportation system, and the controller can maintain stability in the absence of detailed information of the plant. These intelligent control algorithms were experimentally validated to perform well in dealing with non-linear, external disturbances and uncertainties. However, MLTTD is equipped with a load cell for measuring tension force. That is to say, the external disturbance, i.e., the tension force, can be known by the load cell. This makes it possible to employ a simpler control algorithm to compensate for the tension force.

Therefore, feedback linearization [21] was employed in this paper to address this issue. The essential idea of feedback linearization is to decouple a nonlinear system into a pseudo-linear system by the mean of nonlinear state feedback, and then use a linear controller to deal with the pseudo-linear system. However, among all kinds of cases [22]–[25] that apply feedback linearization to maglev systems, most of them focused on the individual control of single-DoF magnetic levitation, i.e., decentralized control. However, since there is coupling between the degrees of freedom in multi-DoF maglev systems, decentralized control tends not to cope well with multi-DoF magnetic levitation systems [26]. On the contrary, the feedback linearization algorithm proposed in this paper is for centralized control of the 2-DoF magnetic levitation. In addition, paper [21] demonstrated that feedback linearization requires accurate plant models. Nevertheless, this paper proposed a tuning method to make the centralized feedback linearization control not rely on an accurate plant model. The proposed feedback linearization control algorithm achieved satisfactory control performance by the tuning method.

As is well known, one of the essential functions of mechanical testing is to obtain the stress-strain curve of a specimen, which requires knowledge of the load applied to the specimen and the deformation of the specimen. Another advantage of using maglev technology to develop a mechanics testing device is that the deformation of the specimen can be indirectly deduced from the magnetic force. Since the specimen is in levitation, its deformation must be reflected in the change amount of airgap, and the airgap is mapped to the coil current and the magnetic force. The current is known because it is the input of the maglev system. Therefore, the deformation of the specimen can be obtained by measuring the magnetic force. Moreover, the magnetic force itself is the load applied to the specimen. In other words, the load applied to the specimen and the deformation of the specimen can be obtained simultaneously by singly measuring the magnetic force. However, even though Maxwell's electromagnetic equation describes the mapping relationship among magnetic force, current, and

TABLE 1. Main components of MLTTD.

| No.	Name	Material/Model	Number
1	Eddy current sensor	SENTEC HA-80R	2
2	Top floator	SS400	2
3	Fixture	A6063	2
4	Bottom floator	SS400	2
5	Aluminum Profile	A6063	3
6	Top EM core	SS400	2
7	Bottom EM core	SS400	2
8	Coil winding	UEW Copper coil	6
9	Load cell	NEC 9E01-L35	1
10	Sealed container	Virtual	1
11	Specimen	SUS304	1
12	Bottom bolt	SS400	1
13	Iron sheet	SS400	1
14	Aluminum sheet	A6063	1
15	Top bolt	SS400	1
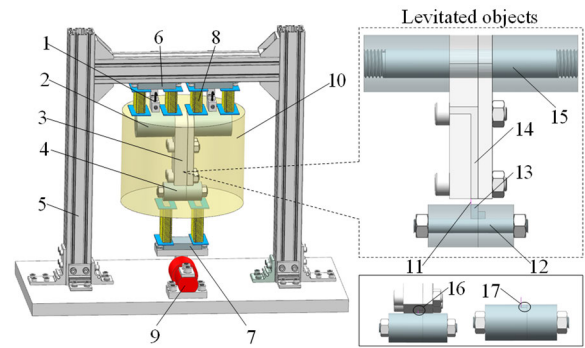
FIGURE 1. Initial structure of MLTTD.

airgap, the equation does not accurately match the actual model of magnetic force, because the actual model contains lots of uncertainties. To solve this problem, a support vector machine (SVM) [27] was employed to build a model that reflects the mapping relationship between the magnetic force, current and airgap.

This paper proceeds as follows. Chapter II proposes the initial structure of MLTTD, discusses the existing problem on the initial structure, and gives design objectives. Chapter III, IV, V investigate the issues raised in Chapter II, and offer solutions or improvements. Chapter III optimize the structure to guarantee the alignment of tension force, the range of tension force. Chapter IV proposes the centralized feedback linearization control algorithm and the tuning method. Chapter V presents the SVM-based model for estimating specimen elongation. Chapter VI presents two kinds of experiments to verify the proposed control algorithm. Chapter VII provides a summary and some extensions of this paper.

The contribution of this paper is as follows:

1. A non-contact tension testing device, where a specimen can be tested while it is levitating, was developed based on magnetic levitation technology.

2. A centralized feedback linearization control algorithm was proposed for the magnetic levitation system, and a tuning method for the control algorithm was proposed to deal with the mismatches between the controller and the plant.

3. A SVM model, which is expected to replace a displacement sensor to measure the specimen elongation, was built.

II. PROBLEM DESCRIPTION
A. INITIAL STRUCTURE
The initial structure of MLTTD is shown in Fig. 1, and the main components of MLTTD are listed in Table 1. As shown in Fig. 1 and Table 1, two electromagnets (EM), called top EMs, were fixed at the top of the framework, and one EM, called bottom EM, was fixed at the bottom of the framework by a load cell. The currents of the three EMs were controlled individually by three controllers. The levitated objects are in the middle of MLTTD, and they include two top floators, one

top bolt, two fixtures, two bottom floators and one bottom bolt were. Among the levitated objects, the two top floators were connected by a bolt named top bolt, and the fixtures were clamped in the middle by the two top floators. An aluminum sheet with 1mm thickness, was embedded in the fixtures and clamped by four threads on the fixtures. Similarly, the two bottom floators were connected by a bottom bolt, and two nuts clamped two bottom floators on both sides of the bottom bolt. An iron sheet with 1mm thickness, was embedded in the bottom floators and clamped by the two nuts. As marked by the NO.16 and NO.17 in Fig. 1, the two ends of the specimen were placed in the slit of the fixtures and the slit of the bottom floators respectively, where the aluminum sheet and the iron sheet press the two ends of the specimen respectively. The advantage of this clamping way is avoiding the slippage of the specimen in horizontal direction.

The working principle of MLTTD is, firstly, the two top EMs, whose currents are controlled individually, attract the two top floators respectively. The two eddy current sensors feed the position of the two top floators to a controller, which then adjusts the currents of the two top EMs to maintain the top floators and the fixtures in a constant vertical position. Subsequently, the bottom EM is electrified, and generates a tension force on the bottom floators, and the current of the bottom EM gradually increases while the top floators and the fixtures maintain in the original position until the specimen is destroyed. The load cell measures the tension force for recording, and also for control feedback, the details of the control will be described in Chapter IV.

B. EXISTING PROBLEMS AND DESIGN OBJECTIVES
However, there are many problems with the initial structure, which can be summarized as follows.

1) ALIGNMENT OF THE TENSION FORCE
As shown in Fig. 2, to simplify the structure, it was not planned to arrange a displacement sensor and an active controller for the bottom floator and the bottom EM. However, due to the lack of active control, tilting will probably occur on the current bottom floator. This will cause the tension force to deviate from the vertical direction, and impact the levitation
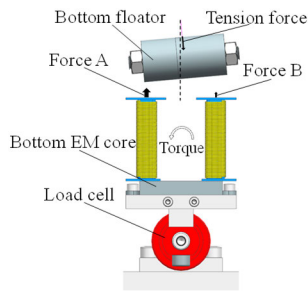
FIGURE 2. An illustration of the misalignment of the tension force.

TABLE 2. Specification of the specimen.

Item	value
Material	SUS304
Tensile yield strength	310 MPa
Ultimate tensile strength	620 MPa
Percent elongation	40%-60%
Diameter of cross-section	0.3mm
Effective Length	4mm

stability. In addition, as the left and right airgaps are different, forces A and force B will be different, this will generate a torque on the load cell, and this torque will disturb the force measurement.

2) THE RANGES OF THE BOTTOM AIRGAP AND THE TENSION FORCE

We used SUS304 as specimen. If the device is successfully designed with SUS304, the device will also be suitable for most other materials, because SUS304 has high strength and good ductility. Table 2 present the specification of the specimen. The dimensions of the specimen were fixed, according to the percent elongation and effective length in Table 2, the specimen will extend approximately 1.6mm to 2.4mm after being destroyed, so the airgap between bottom EM and bottom float, which is named bottom airgap, should be larger than 2.4mm. According to the ultimate tensile strength, a tensile force of at least 43.82 N is required to destroy such a specimen. For insurance purposes, it was specified that the airgap between the bottom EM core and the bottom floaters should be at least 4mm and MLTTD should produce at least 50N tension force. In addition, to obtain as complete a stress-strain curve as possible, it is best if the tension force can be loaded from 0N. However, due to the weight of the bottom floaters, it is impossible to load the tension force from 0N. Therefore, the second best, the bottom floater should be as light as possible.

3) LEVITATION CONTROL

As described before, the levitation of the two top floators are controlled by the two top EMs, this may be easy. However, after tension force is loaded, to maintain the levitation, it is necessary to consider suppressing the disturbance caused by the tension force.

4) MEASUREMENT OF SPECIMEN ELONGATION

A material mechanics testing device needs to measure both loading force and specimen elongation to obtain stress-strain curve. In MLTTD, the load cell can indirectly measure the loading force. The elongation is equal to the amount of change in the bottom airgap. Moreover, the bottom airgap can be calculated according to Eq (2), Eq (2) is transformed from Eq (1), which describes the magnetic force of an electromagnet.

$$F = \frac{ai^2}{(z+c)^2} \tag{1}$$

$$z = \sqrt{\frac{ai^2}{F}} - c \tag{2}$$

where, F is magnetic force, i is the current of electromagnetic coil, z is equivalent airgap. a and c are constants depending on the physical parameters of electromagnet and floator. As F can be measured by the load cell and i can be obtained from the controller's output, so as long as a and c are caught, z can be got without a displacement sensor. In this way, the mounting of displacement sensor in the bottom can be omitted, simplifying the structure. However, using Eq (2) does not address this issue effectively, because there are lots of uncertainties in actual magnetic model, such as magnetic saturation, model errors, and time-varying factors. So, it is an unsolved problem.

5) DESIGN OBJECTIVES

According to the above existing problems, improvement was necessary. Therefore, design objectives were proposed as follows:

1. To simplify the structure, alignment of the tension force should be ensured even in the absence of an active controller.

2. The bottom airgap is initially set to 4mm, leaving sufficient space for the specimen elongation. With 4mm airgap, the bottom EM should be able to produce at least 50N attractive force on the bottom floators.

3. To obtain as complete stress-strain curve as possible, the weight of the bottom floator should be lower than 5N.

4. To suppress the disturbance caused by the tension force, the controller for levitation should have stronger robustness than regular linear controller.

5. To simplify the structure, measurement of the specimen elongation should be realized by an estimation method instead of a displacement sensor, and the RMSE of estimation should be within 0.1mm.

III. IMPROVEMENT OF THE STRUCTURE

Given the structure shown in Fig. 2 there is a risk of misalignment of the tension force, and it is necessary to modify the structure of the bottom floaters and the bottom EM. As shown in Fig. 3, three different shapes of floators were considered as alternatives to avoid the tilting of the bottom floaters. Also, the U-shape EM was replaced by a cylindrical EM because the magnetic force produced by cylindrical EM is
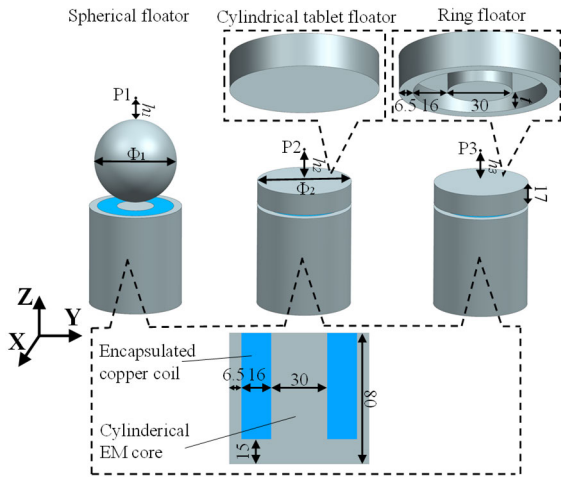
FIGURE 3. Three different shapes of floators.

more concentrated. The cylindrical EMs were identical in the three cases. In order to investigate the magnetic characteristics of the three floators and determine which one is best for the alignment of tension force, using J-Mag software, the magnetic forces and magnetic torques of the cylindrical EM to the three floators were respectively studied in different positions of the three floators. Over the J-Mag analyses, the cylindrical floator was fixed while the positions of the three floats were variable. And the type of all the J-mag analyses was transient, so the change in positions of the three floators did not represent that the floator had velocity or motion. In addition, the number of coil turns was set to 700. Since a 0.8mm diameter copper coil was expected to be used to make the cylindrical EMs, and the coil current was set to 4.085A, which is the rated current of the 0.8mm copper coil. The airgaps between the floators and the cylindrical EM were set to 4mm.

The analysis results are shown in Fig. 4, Fig. 5 and Fig. 6. Overall results, a horizontal coordinate of 0 means that the floator was in its original position, i.e., the position where the floator and cylindrical EM are co-axial. The legend Φ_1 in Fig. 4(a) and Fig. 4(b) denotes the diameters of the spherical floator while the legend Φ_2 in Fig. 5(a) and Fig. 5(b) denotes the diameters of the cylindrical table floator, the dimensions Φ_1 and Φ_2 are illustrated in Fig. 3. In the analysis of Fig. 4(c), Fig. 5(c) and Fig. 6(c), the angular positions of the three floators varied around point P1, point P2 and point P3 (illustrated in Fig. 3) respectively, which were also the bases for calculating the magnetic torques of the cylindrical electromagnet to the floators respectively; the legends h_1, h_2, h_3 (illustrated in Fig. 3) represent the vertical distance from P1, P2, P3 to the upper surfaces of the corresponding floators respectively, the dimensions h_1, h_2, h_3 determine the positions of point P1, point P2 and point P3 respectively. The physical meaning of P1, P2, P3 will be given later. In Fig. 6(a) and Fig. 6(b), legend t denotes the depth of the groove of the ring floator, the dimension t is illustrated in Fig. 3.

As shown in Fig. 4(a), to obtain a tension force greater than 50N, at least 70mm diameter of the spherical floator is required. In addition, Fig. 4(b) shows that the slopes of all the curves are negative, which means all the cases can produce a recovery force to prevent the floators from lateral movement. In other words, all the floators in Fig. 4(b) are passively controllable in horizontal direction. Therefore, based on this result, the floator with diameter of 70mm was chosen to conduct the analysis in Fig. 4(c). Likewise, Fig. 4(c) shows that the slopes of all the curves are negative, which implies that the 70mm spherical floator can produce a recovery torque to prevent itself from tilting no matter where the rotation center is. In other words, the movement of the 70mm spherical floator around the horizontal axis is passively controllable.

To sum up, Fig 4(b) and Fig. 4(c) indicate that 70mm spherical floator can ensure the alignment of the tension force even in the absence of an active controller. These may seem perfect. However, 70mm spherical floator weighs about 13.02N, and the force required to destroy the specimen is about 43.82 N. That is to say, such a mass is too heavy to obtain a completed stress-strain curve. Therefore, the spherical floator was abandoned.

As shown in Fig. (5), the similar analysis was conducted for the cylindrical tablet floator. Fig. 5(a) demonstrates that a at least 40mm diameter of the cylindrical tablet floator is required to produce a tension force more than 50N. However, Fig. 5(b) implies that the 40mm cylindrical tablet floator is not passively controllable in horizontal direction, because the slopes of the corresponding curve is positive. Therefore, the diameter was increased to 70mm for the analysis in Fig. 5(c). Nevertheless, the slopes of all the curves in Fig. 5(c) imply that this floator cannot prevent itself from tilting no matter where the rotation center is. Hence, the cylindrical tablet floators was also abandoned.

It was found that a ring floator with the same cross-section as the cylindrical EM combines both the advantages of the spherical floator and the cylindrical tablet floator. Its cross-section dimensions are shown in Fig. 3. Similar analysis for this floator was conducted and the results are shown in Fig. 6. Fig. 6(a) and 6(b) respectively display the curves of vertical and horizontal magnetic force of the cylindrical EM to the ring floator under different values of t. Fig. 6(a) shows that all the cases can generate much more than 50N tension force. Furthermore, as can be seen in Fig. 6(b), the slopes of all the curves are negative, which implies that all the cases can prevent the floator from lateral displacement. Based on the results in Fig. 6(a) and Fig. 6(b), and considering the ease of the installation of the floator, the value of t was selected as 8mm, and this value was used to conduct the analysis in Fig. 6(c). Fig. 6(c) shows that this floator can prevent itself from tilting only when h_3 is greater than 20mm, so the value of h_3 was selected as 40mm to get enough recovery torque. In fact, as shown in Fig. 7, the physical meaning of h_3 is the distance from the upper end of the specimen to the upper surface of the floator, and the upper end of the specimen is point P3, which is also illustrated in Fig. 3. h_3 can be
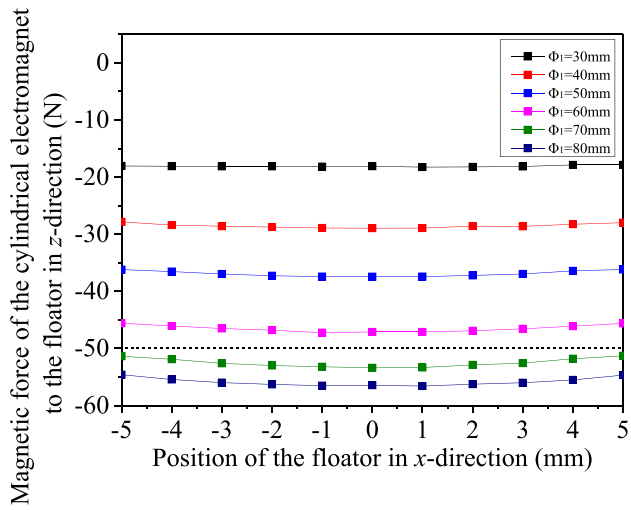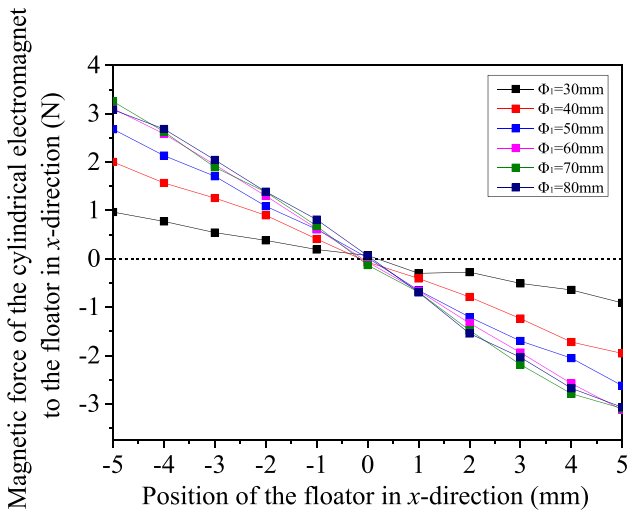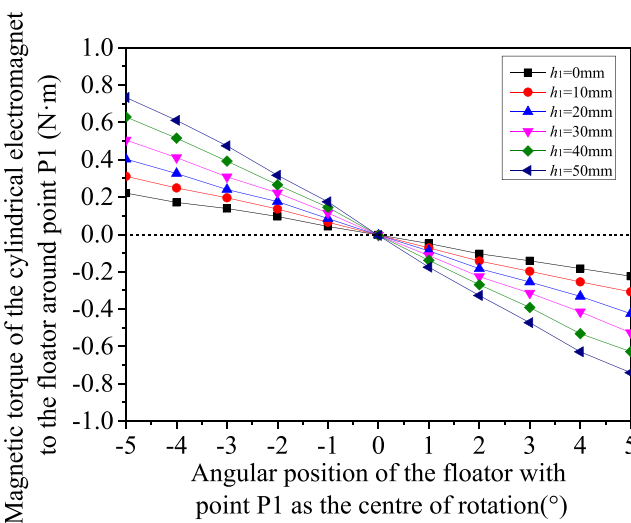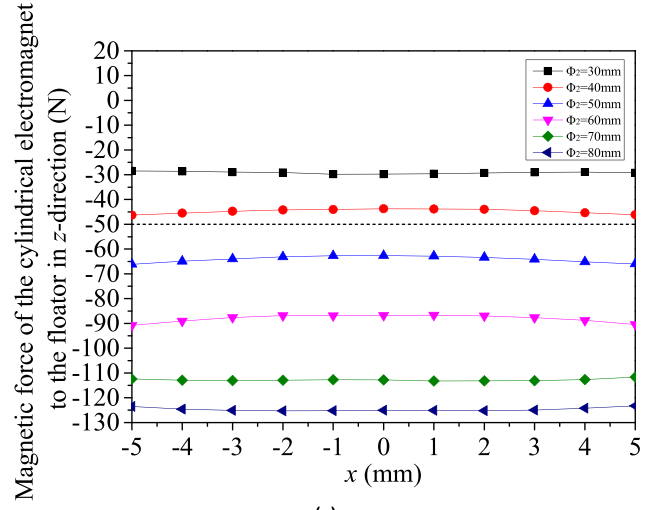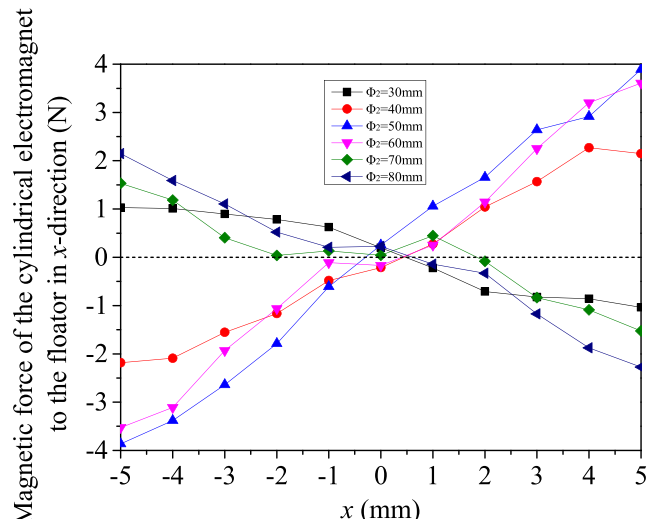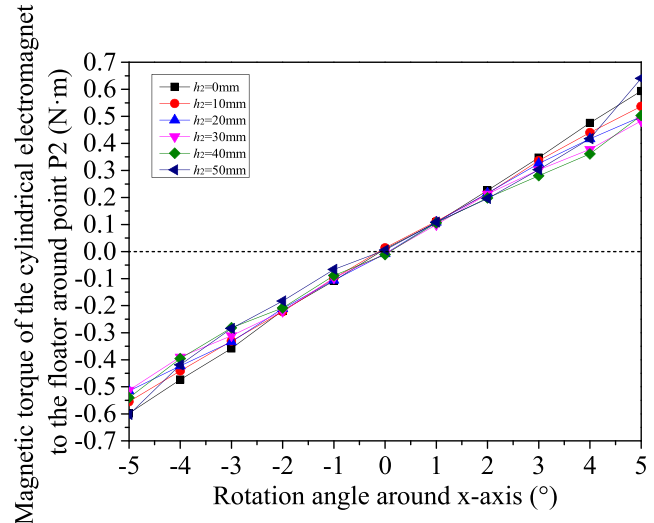
FIGURE 4. J-Mag analysis results of the spherical floator.

FIGURE 5. J-Mag analysis results of the cylindrical tablet floator.

TABLE 3. Specification of MLTTD after improvement.

d (mm)	50
e (mm)	60
f (mm)	40
h_3 (mm)	40
Number of turn per top coil	260
Number of turn of the bottom coil	600
Top airgaps (mm)	2
Bottom airgap (mm)	4
Range of tension force (N)	4.97 to 82.34

adjusted by designing an appropriate fixture. As mentioned in Chapter II-B-1), due to lack of active control, the floator is likely to rotate around point P3 during tensioning process, similarly, this is also the reason why h_1 and h_2 were set to the variables in the analysis of Fig. 4(c) and Fig. 5(c) respectively to investigate the magnetic torques. To sum up Fig. 6(b) and Fig. 6(c), the alignment of the tension force can be ensured by employing the ring floator and designing an appropriate fixture even in the absence of an active controller.

Therefore, the ring floator with $t = 8$ was finally selected. Furthermore, according to the analysis of Fig. 6(c), a fixture named bottom fixture, which is shown in Fig. 7, was designed to make $h_3 = 40$. Finally, the total weight of the ring floator and the bottom fixture was only 4.97N.

Moreover, another J-Mag analysis was performed to minimize the heights of the cylindrical EM core, the fixture and the top EM core, which are illustrated by d, e, f respectively in Fig. 7. In addition, the numbers of turn of all the coil windings were minimized. All the minimizations were conducted while ensuring sufficient tension force. The improved structure is presented in Fig. 8, all the parts that were named or renamed are marked. Furthermore, the specification of the improved structure is presented in Table 3.

IV. CONTROL OF THE LEVITATION

About the control of magnetic levitation, linear control algorithms such as PD and PID are widely used. However, these linear control algorithms are based on the linearization around an equilibrium point where the magnetic force exactly counteracts the gravity of a levitated object. As a result, once the current or airgap deviates far from the bias current or equilibrium airgap, these linear control algorithms will lose their original performance and even fail to maintain levitation. For MLTTD, to compensate for a continuously increasing tension force, it is necessary to make the top EMs work over a wide range of currents. Therefore, traditional linear control algorithms are not suitable. To address this problem, a nonlinear mathematical model was built and a 2-DoF centralized feedback linearization control algorithm was proposed based on the nonlinear mathematical model.

A. A NONLINEAR MATHEMATICAL MODEL FOR MLTTD
To start, a mathematical model for the levitation was built. As illustrated in Fig. 9, i_1 and i_2 are the currents of the two
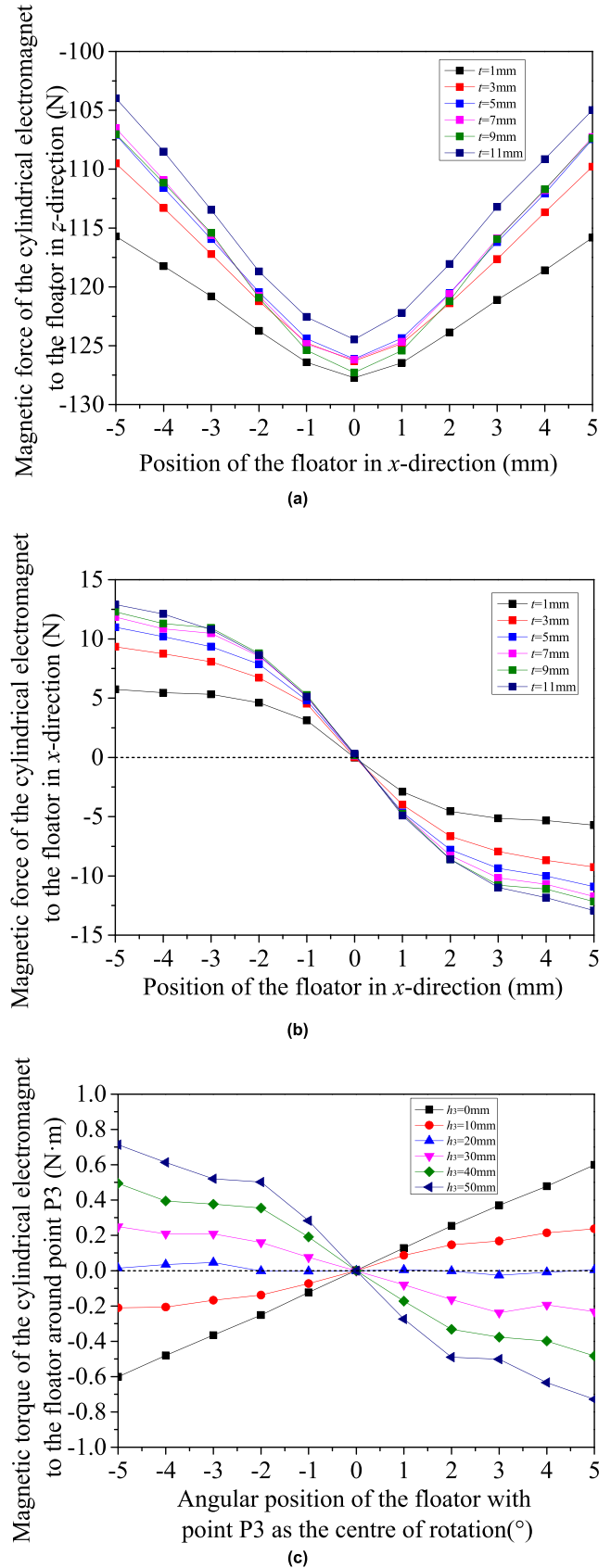

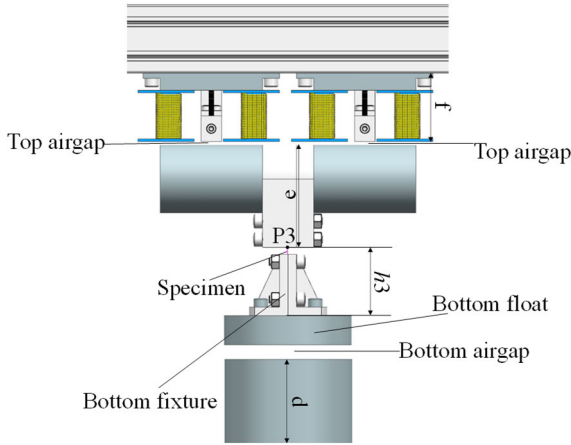**FIGURE 6.** J-Mag analysis results of the ring floator.

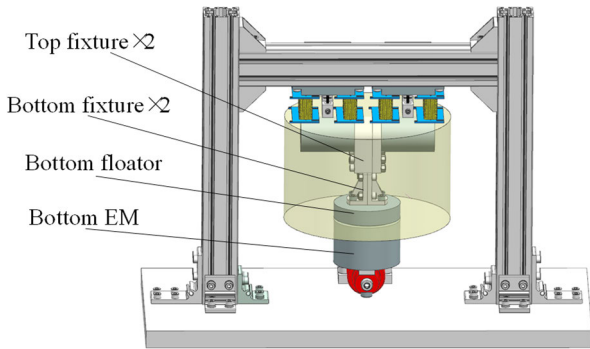**FIGURE 7.** The physical meaning of $h3$.

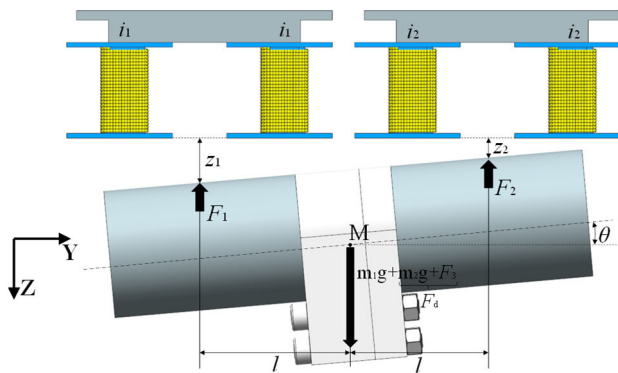**FIGURE 8.** MLTTD after improvement.

FIGURE 9. Illustrations of the mathematical model.

coil windings, z_1 and z_2 are the two equivalent airgaps, F_1 and F_2 are the attractive force of the two top EMs to the two top floators while F_3 is the attractive force of the bottom EM to the bottom floator. m_1 is the total mass of the top floators and the top fixtures while m_2 is the total mass of the bottom floator and the bottom fixture. θ is the rotation angle of the top floators. Point M is resultant center of mass (COM) of the top floators and the top fixtures. Consider i_1 and i_2 as inputs, z_1 and z_2 as outputs. According to the dynamics of plane motion

of a rigid body. the dynamics equation of the top floators and the top fixtures can be described as Eq (3).

$$\begin{cases} m_1 g - (F_1 + F_2) = \ddot{z}_M \\ (F_2 - F_1)l = J\ddot{\theta} \end{cases} \tag{3}$$

where, z_M is the vertical displacement of the resultant COM of both the top floators and the top fixtures, and z_M is equal to $\frac{z_1+z_2}{2}$. J is the momentum of inertia of the resultant mass of the top floators and the top fixtures around the resultant COM of both the top floators and the top fixtures. It can be assumed that $\ddot{\theta} \approx tan\theta = \frac{\ddot{z}_1 - \ddot{z}_2}{2l}$, because θ is small. Substituting $z_M = \frac{z_1+z_2}{2}$ and $\ddot{\theta} \approx \frac{\ddot{z}_1 - \ddot{z}_2}{2l}$ into Eq (3), yields:

$$\begin{cases} m_1 g - (F_1 + F_2) = m_1 \dfrac{\ddot{z}_1 + \ddot{z}_2}{2} \\ (F_2 - F_1)l = J\dfrac{\ddot{z}_1 - \ddot{z}_2}{2l} \end{cases} \tag{4}$$

Substituting $F_1 = \frac{ai_1^2}{(z_1+c)^2}$ and $F_2 = \frac{ai_2^2}{(z_2+c)^2}$ into Eq (4), yields:

$$\begin{cases} m_1 g - \left(\dfrac{ai_1^2}{(z_1+c)^2} + \dfrac{ai_2^2}{(z_2+c)^2} \right) = m_1 \dfrac{\ddot{z}_1 + \ddot{z}_2}{2} \\ \dfrac{-lai_1^2}{(z_1+c)^2} + \dfrac{lai_2^2}{(z_2+c)^2} = J\dfrac{\ddot{z}_1 - \ddot{z}_2}{2l} \end{cases} \tag{5}$$

Organizing Eq (5), yields:

$$\begin{cases} 2g - \left(\dfrac{2ai_1^2}{m_1(z_1+c)^2} + \dfrac{2ai_2^2}{m_1(z_2+c)^2} \right) = \ddot{z}_1 + \ddot{z}_2 \\ \dfrac{-2l^2ai_1^2}{J(z_1+c)^2} + \dfrac{2l^2ai_2^2}{J(z_2+c)^2} = \ddot{z}_1 - \ddot{z}_2 \end{cases} \tag{6}$$

Letting the two equations in Eq (6) be added together, obtains:

$$\ddot{z}_1 = g - \frac{a}{m_1}\left(\frac{i_1^2}{(z_1+c)^2} + \frac{i_2^2}{(z_2+c)^2} \right) \\ + \frac{l^2 a}{J}\left(-\frac{i_1^2}{(z_1+c)^2} + \frac{i_2^2}{(z_2+c)^2} \right) \tag{7}$$

Letting the two equations in Eq (6) be subtracted, obtains:

$$\ddot{z}_2 = g - \frac{a}{m_1}\left(\frac{i_1^2}{(z_1+c)^2} + \frac{i_2^2}{(z_2+c)^2} \right) \\ - \frac{l^2 a}{J}\left(-\frac{i_1^2}{(z_1+c)^2} + \frac{i_2^2}{(z_2+c)^2} \right) \tag{8}$$

Then, define state variable $[x_1; x_2; x_3; x_4]$ of the plant as follows:

$$\begin{cases} x_1 = z_1 + c \\ x_2 = \dot{z}_1 \\ x_3 = z_2 + c \\ x_4 = \dot{z}_2 \end{cases} \tag{9}$$

Then, the state equation of the plant can be written as follows:

$$
\begin{cases}
\dot{x}_1 = x_2 \\
\dot{x}_2 = \ddot{z}_1 \\
\dot{x}_3 = x_4 \\
\dot{x}_4 = \ddot{z}_2
\end{cases}
\tag{10}
$$

Substituting Eq (7) and Eq (8) into Eq (10), yields:

$$
\begin{cases}
\dot{x}_1 = x_2 \\
\dot{x}_2 = g - \dfrac{a}{m_1}\left(\dfrac{i_1^2}{x_1^2} + \dfrac{i_2^2}{x_3^2}\right) + \dfrac{l^2 a}{J}\left(-\dfrac{i_1^2}{x_1^2} + \dfrac{i_2^2}{x_3^2}\right) \\
\dot{x}_3 = x_4 \\
\dot{x}_4 = g - \dfrac{a}{m_1}\left(\dfrac{i_1^2}{x_1^2} + \dfrac{i_2^2}{x_3^2}\right) - \dfrac{l^2 a}{J}\left(-\dfrac{i_1^2}{x_1^2} + \dfrac{i_2^2}{x_3^2}\right)
\end{cases}
\tag{11}
$$

Define the input $[u_1; u_2]$ of the plant as follows:

$$
\begin{cases}
u_1 = i_1^2 \\
u_2 = i_2^2
\end{cases}
\tag{12}
$$

Substituting Eq (12) to Eq (11), yields:

$$
\begin{cases}
\dot{x}_1 = x_2 \\
\dot{x}_2 = g - \dfrac{a}{m_1}\left(\dfrac{u_1}{x_1^2} + \dfrac{u_2}{x_3^2}\right) + \dfrac{l^2 a}{J}\left(-\dfrac{u_1}{x_1^2} + \dfrac{u_2}{x_3^2}\right) \\
\dot{x}_3 = x_4 \\
\dot{x}_4 = g - \dfrac{a}{m_1}\left(\dfrac{u_1}{x_1^2} + \dfrac{u_2}{x_3^2}\right) - \dfrac{l^2 a}{J}\left(-\dfrac{u_1}{x_1^2} + \dfrac{u_2}{x_3^2}\right)
\end{cases}
\tag{13}
$$

Eq (13) is the nonlinear state space model of the plant, for ease of description, Eq (13) was rewritten as follows:

$$
\begin{cases}
\dot{x}_1 = x_2 \\
\dot{x}_2 = f_1\,(x_1, x_3, u_1, u_2) \\
\dot{x}_3 = x_4 \\
\dot{x}_4 = f_2\,(x_1, x_3, u_1, u_2)
\end{cases}
\tag{14}
$$

B. CENTRALIZED FEEDBACK LINEARIZATION

Then, as mentioned in the Introduction of this paper, a centralized feedback linearization control algorithm was employed to deal with the nonlinear system. The derivation process of the centralized feedback linearization control algorithm is shown as follows:

Let

$$
\begin{cases}
f_1\,(x_1, x_3, u_1, u_2) = v_1 \\
f_1\,(x_1, x_3, u_1, u_2) = v_2
\end{cases}
\tag{15}
$$

Treating u_1 and u_2 as two unknows of Eq (15), and solving Eq (15), yields:

$$
\begin{cases}
u_1 = \dfrac{x_1^2}{2a}\left[m_1 g - \dfrac{m_1\,(v_1 + v_2)}{2} - \dfrac{J\,(v_1 - v_2)}{2l^2}\right] \\
u_2 = \dfrac{x_3^2}{2a}\left[m_1 g - \dfrac{m_1\,(v_1 + v_2)}{2} + \dfrac{J\,(v_1 - v_2)}{2l^2}\right]
\end{cases}
\tag{16}
$$

Substituting Eq (15) into Eq (14), Eq (17) is obtained. So, Eq (16) are control laws that convert the nonlinear system represented by Eq (14) into a pseudo-linear system represented by Eq (17).

$$
\begin{cases}
\dot{x}_1 = x_2 \\
\dot{x}_2 = v_1 \\
\dot{x}_3 = x_4 \\
\dot{x}_4 = v_2
\end{cases}
\tag{17}
$$

where v_1 and v_2 were treated as the input of the pseudo-linear system. Next, it is a simple matter to design the appropriate feedback gains $\beta_1, \beta_2, \beta_3$ and β_4 for the pseudo-linear system, i.e.,

Let

$$
\begin{cases}
v_1 = \beta_1 e_1 + \beta_2 e_2 \\
v_2 = \beta_3 e_3 + \beta_4 e_4
\end{cases}
\tag{18}
$$

where

$$
\begin{cases}
e_1 = 0.002m - z_1 \\
e_2 = -\dot{z}_1 \\
e_3 = 0.002m - z_2 \\
e_4 = -\dot{z}_2
\end{cases}
\tag{19}
$$

Finally, substituting Eq (18) into Eq (16), and replace u_1, u_2, x_1, x_2 with i_1^2, i_2^2, $z_1 + c$, $z_2 + c$, the control currents are obtained as Eq (20), as shown at the bottom of the next page. where, i_1 and i_2 are the currents of the two top EMs, z_1 and z_2 are the two top airgaps, e_1 and e_3 are the errors of the two top airgaps, e_2 and e_4 are the errors of the differentiations of the two top airgaps. In addition to them, there are two kinds of constant parameters, which determine the control performance. One belongs to the feedback gains, they are β_1, β_2, β_3, β_4; the other one belongs to the plant parameters, they are m_1, g, J, l, a, c. The feedback gains can be obtained via LQR method [28]. In addition, [21] argued that although feedback linearization gives excellent performance, it requires accurate plant models. This means that the excellent control performance can only be achieved when the plant parameters in Eq (20) are precisely matched to the plant model. However, it is difficult to get an accurate plant model for a maglev system because there is much inherent uncertainty in a maglev system. Therefore, it is necessary to investigate the impact of the mismatch of the plant parameters on the control system. The mismatch means that the values of m_1, g, J, l, a, c in the control law shown by Eq (20) deviate from the values of m_1, g, J, l, a, c in the plant. For ease of observation, let $d = \frac{J}{m_1 l^2}$ Eq (20) can be rewritten to Eq (21), as shown at the bottom of the next page. Finally, there were totally five plant parameters, they were m_1, g, d, a, c. Among these parameters, m_1 can be accurately weighed by an electronic scale, which has an accuracy of 0.1 gram. So, there were four plant parameters remained to be studied, they are g, d, a, c, which will be further investigated in Chapter IV-C.
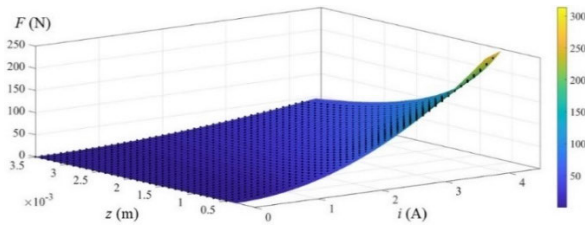
FIGURE 10. J-Mag analysis result and fitting surface.

C. CONTROL SIMULATION

To investigate the impact of the mismatch of the four parameters on the control system. Electromagnetic analysis and control simulations were performed using J-Mag and MATLAB-Simulink respectively. The J-Mag analysis is for getting reference values of parameter a and c. In the J-Mag analysis, set both i_1 and i_2 to synchronously vary from 0.1A to 4.2A in 0.1A step, set both z_1 and z_2 to synchronously vary from 0.5mm to 3.5mm in 0.1mm step. The J-Mag analysis result is shown in Fig. 10, where $F = F_1 + F_2$, $z_1 = z_2 = z$, $i_1 = i_2 = i$, furthermore the data was fitted in the form of $F = \frac{ai^2}{(z+c)^2}$, obtaining a fitting surface and it was obtained that the reference values of a, c were respectively $3.051 \times 10^{-5} \text{Nm}^2\text{A}^{-2}$ and $1.595 \times 10^{-3}\text{m}$ for a single top EM. In addition, the reference values of m and d were 1.434kg and 1.031, which were calculated out according to the density of the material and the volume. g is the acceleration of gravity and the corresponding reference value was 9.807m/s^2.

Fig. 11 give an illustration of control diagram in the control simulations. All the controllers in Fig. 11 are consistent with Eq (21). As shown in Fig. 11(a), when there is no tension force, only the controller is enough. However, as shown in Fig. 11(b), tension force F_3 and the weight of the lower floators m$_3$g will form a disturbance F_d on the system, and it was assumed that F_d acts on the point M. Therefore. it is necessary to compensate the disturbance. The preliminary approach presented in paper [29] was to use the load cell to configure a force feedback path shown in Fig. 11(c), which employs two same constant force feedback gains. However, this method was proposed based on a simplified linear model, which neglected the non-linearity of the maglev system. And as mentioned before, in the process of applying tension force,

the currents of the top EMs will continuously increase to maintain the levitation, so the plant model will inevitably deviate away from the original plant model. In other words, as the currents of the top EMs increase continuously, the inherent non-linearity of the magnetic levitation system will appear, the constant force feedback gains will no longer fit the plant model after the deviation. Therefore, an improved method shown in Fig. 11(d) was proposed. Comparing with Fig. 11(c), Fig. 11(d) shows a dynamic force feedback gains instead of the constant force feedback gains. As shown in Fig. 11(d), the dynamic force feedback gains consist of a superpositions of the proportion and integral of airgap errors. Finally, the control simulations were conducted using the control diagram in Fig. 11(d). Table 4 gives the simulation settings and Fig. 12 shows the simulation results. The model mismatch was simulated by parameter fluctuations in the controller, and the fluctuation range of g, d, a, c values in the controller are given in blue in Table 4, Since it is impossible to list all the values in the fluctuation range, among Fig. 12(b), Fig. 12(c), Fig. 12(d) and Fig. 12(e), each graph only shows one of the cases, they are g = 9.78 m/s^2, d = 1.933, a = $2.4408 \times 10^{-5}\text{Nm}^2\text{A}^{-2}$, c = 1.276×10^{-3} m respectively. Actually, when these four parameters take other values in their fluctuation range, the simulation results were basically the same as that of Fig. 12(b), Fig. 12(c), Fig. 12(d) and Fig. 12(e). In other words, Fig. 12(b), Fig. 12(c), Fig. 12(d) and Fig. 12(e) are the results that can represent all cases in the fluctuation ranges. Furthermore, to check the dynamic performance of the controller, 1mm step disturbance was applied to z_1 and z_2 at 1.5 seconds and 3 seconds respectively. In addition, at 5 seconds, F_d was applied to the system, where F_3 was a ramp force with a 10N/s slope while m$_2$g was 2.82N, and the upper limit of F_d was set to 50N.

Fig. 12(a) present the simulation result where all the parameters in the plant model and the controller are identical, Fig. 12(b), Fig. 12(c), Fig. 12(d) and Fig. 12(e) present the simulation results where the g, d, a, c in the controller mismatch the g, d, a, c in the plant model respectively. Over these five graphs, it can be observed that only the mismatch of c and a have significant impacts on the control performance. Fig. 12(d) and Fig. 12(e) imply that the mismatch of a and c caused a steady-state error on the airgaps before applying F_d, and weakened the robustness of the control system to F_d.

$$\begin{cases} i_1 = \sqrt{\dfrac{(z_1 + c)^2}{2a}\left[\text{m}_1\text{g} - \dfrac{\text{m}_1\left(\beta_1 e_1 + \beta_2 e_2 + \beta_3 e_3 + \beta_4 e_4\right)}{2} - \dfrac{J\left(\beta_1 e_1 + \beta_2 e_2 - \beta_3 e_3 - \beta_4 e_4\right)}{2l^2}\right]} \\ i_2 = \sqrt{\dfrac{(z_2 + c)^2}{2a}\left[\text{m}_1\text{g} - \dfrac{\text{m}_1\left(\beta_1 e_1 + \beta_2 e_2 + \beta_3 e_3 + \beta_4 e_4\right)}{2} + \dfrac{J\left(\beta_1 e_1 + \beta_2 e_2 - \beta_3 e_3 - \beta_4 e_4\right)}{2l^2}\right]} \end{cases} \quad (20)$$

$$\begin{cases} i_1 = \sqrt{\dfrac{\text{m}_1(z_1 + c)^2}{2a}\left[\text{g} - \dfrac{\left(\beta_1 e_1 + \beta_2 e_2 + \beta_3 e_3 + \beta_4 e_4\right)}{2} - \dfrac{\text{d}\left(\beta_1 e_1 + \beta_2 e_2 - \beta_3 e_3 - \beta_4 e_4\right)}{2}\right]} \\ i_2 = \sqrt{\dfrac{\text{m}_1(z_2 + c)^2}{2a}\left[\text{g} - \dfrac{\left(\beta_1 e_1 + \beta_2 e_2 + \beta_3 e_3 + \beta_4 e_4\right)}{2} + \dfrac{\text{d}\left(\beta_1 e_1 + \beta_2 e_2 - \beta_3 e_3 - \beta_4 e_4\right)}{2}\right]} \end{cases} \quad (21)$$

TABLE 4. The simulation settings.

Parameters	Values in the plant model	Values in the controller				
		In Fig. 12(a)	In Fig. 12(b)	In Fig. 12(c)	In Fig. 12(d)	In Fig. 12(e)
m_1 (kg)	1.434	1.434	1.434	1.434	1.434	1.434
g (m/s^2)	9.807	9.807	9.78~9.83	9.807	9.807	9.807
d	1.031	1.031	1.031	0.573~1.933	1.031	1.031
a (Nm^{2}A^{-2})	3.051×10^{-5}	3.051×10^{-5}	3.051×10^{-5}	3.051×10^{-5}	2.4408×10^{-5}~3.6612×10^{-5}	3.051×10^{-5}
c (m)	1.595×10^{-3}	1.595×10^{-3}	1.595×10^{-3}	1.595×10^{-3}	1.595×10^{-3}	1.276×10^{-3}~1.914×10^{-3}
β_1	No such item	9800	9800	9800	9800	9800
β_2	No such item	180	180	180	180	180
β_3	No such item	9800	9800	9800	9800	9800
β_4	No such item	180	180	180	180	180
K_{FP}	No such item	2500	2500	2500	2500	2500
K_{FI}	No such item	2500	2500	2500	2500	2500

Furthermore, it was found that the airgaps stepped sharply in the negative direction at the 5s when the steady-state errors were positive before the 5s, and the airgaps stepped sharply in the positive direction at 5s when the steady-state errors were negative before the 5s. Accordingly, it is speculated that the steady-state errors make the initial value of the dynamic force feedback gains shown in Fig. 11(d) at 5s too large, this makes the system too sensitive to F_d. Based on this speculation, as shown in Fig. 13, a hypothesis was raised, i.e., as long as the steady-state values of z_1 and z_2 are 0mm before applying F_d, the system will have good robustness to F_d. If this hypothesis is correct, good robustness of the system to F_d can be achieved by making the steady-state errors be zero before applying F_d, furthermore, if we can propose a method to make the steady-state error zero in the case of mismatch, good robustness to F_d can be achieved even without an accurate plant model. For this purpose, in the following, firstly, a sufficient condition to make the steady-state error zero will be proposed based on theoretical analysis, and then the hypothesis will be verified by simulation.

With regard to the elimination of steady-state error, it is possible to solve it by adding an integrator to the feedback loop, but the integrator probably weakens the dynamic performance of the system. Also, if the steady-state error is large, the integrator is likely to make the system unstable with the original control parameters. While the method proposed in the following to eliminate steady-state error is achieved by tuning the original control parameters a_c and c_c, therefore it is more feasible. The derivation of the tuning method is shown as follows.

The first five seconds of Fig. 12(d) and Fig. 12(e) show that although there were steady-state errors, the two airgaps converged to the same values. Therefore, it can be assumed that $e_1 = e_3 = e_{ss}$, $e_2 = e_4 = 0$ when the system reaches steady state in the condition of the mismatch of a and c, where e_{ss} denotes the steady-state values of e_1 and e_3. Also, it can be assumed that $\beta_1 = \beta_3$, $\beta_2 = \beta_4$ due to the symmetry of the structure. Then Substituting $\beta_1 = \beta_3$, $\beta_2 = \beta_4$, $e_1 = e_3 = e_{ss}$, $e_2 = e_4 = 0$ into Eq (21), the steady-state currents were

obtained as follows:

$$i_e = \sqrt{\frac{m_1 (z_e + c)^2}{2a} (g - \beta_1 e_{ss})} \qquad (22)$$

where, i_e is the steady-state value of i_1 and i_2, z_e is the steady-state value of z_1 and z_2. To distinguish the parameters in the plant and the controller, the parameters a and c in the controller will be written as a_c and c_c, while the parameters a and c in the plant will be remained same as before. Therefore, Eq (22) is rewritten as follows:

$$i_e = \sqrt{\frac{m_1 (z_e + c_c)^2}{2a_c} (g - \beta_1 e_{ss})} \qquad (23)$$

Substituting Eq (23) into $F_e = \frac{a i_e^2}{(z_e + c)^2}$, the magnetic force generated by each EM in steady state is yield as follows:

$$F_e = \frac{a m_1 (z_e + c_c)^2}{2a_c (z_e + c)^2} (g - \beta_1 e_{ss}) \qquad (24)$$

According to Eq (24), the acceleration of the airgaps in steady state can be obtained as follows:

$$\ddot{z}_e = g - \frac{2F_e}{m_1} = g - \frac{a (z_e + c_c)^2}{a_c (z_e + c)^2} (g - \beta_1 e_{ss}) \qquad (25)$$

Replace e_{ss} with 0.002mm-z_e, Eq (25) can be written as:

$$\ddot{z}_e = g - \frac{a (z_e + c_c)^2}{a_c (z_e + c)^2} [g - \beta_1 (0.002\text{mm} - z_e)] \qquad (26)$$

There is no doubt that $\ddot{z}_e$ is equal to 0m/s^2 in steady state. Therefore, z_e can be solved by Eq (27). In addition, $z_e = 0.002$mm is equivalent to the steady-state error of zero, therefore, the issue is transformed to solving for z_e by Eq (27), where only z_e is treated as an unknown independent variable, a, c, a_e, c_e, g, β_1 are treated as the known parameters of the equation.

$$g = \frac{a (z_e + c_c)^2}{a_c (z_e + c)^2} [g + \beta_1 (z_e - 0.002\text{mm})] \qquad (27)$$

Obviously, the solution of this equation depends on the parameters a, c, a_e, c_e, g, β_1. Among these, a, c, g are fixed

(a) Control method in the absence of tension force

(b) Illustration of the disturbance

(c) The constant-gain force feedback control

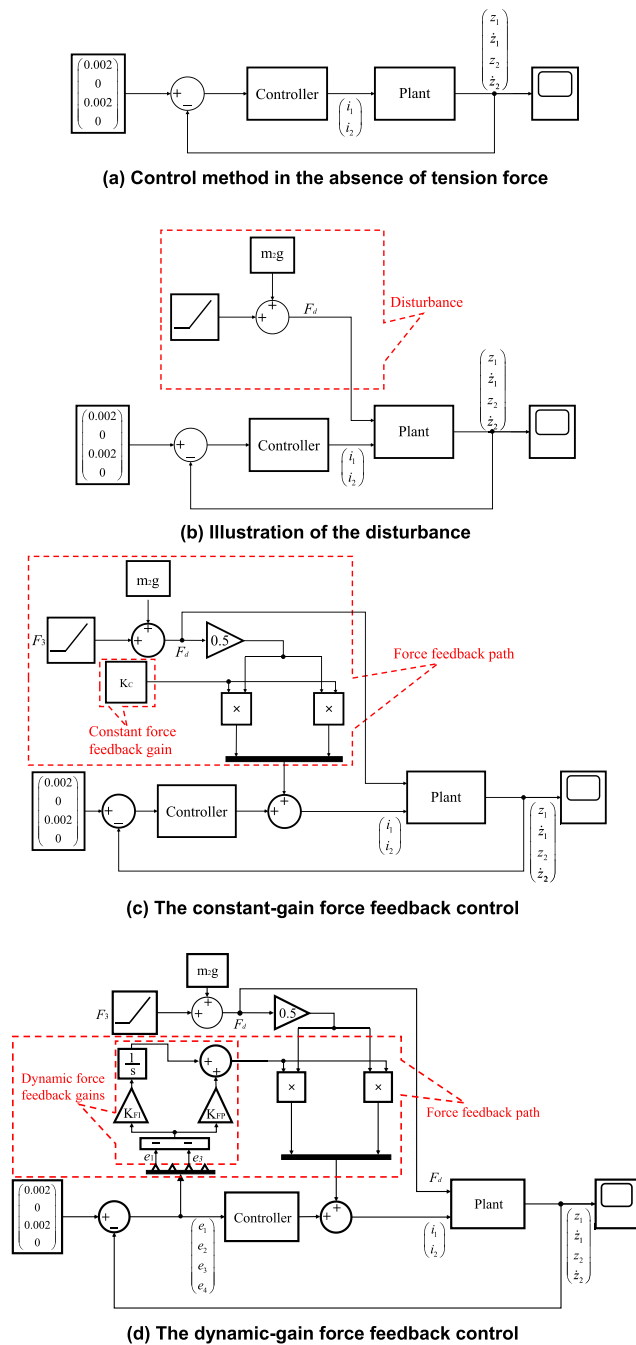**(d) The dynamic-gain force feedback control**

FIGURE 11. Illustration of control diagram in the control simulations.

since they are the parameters of the plant model. For the sake of analysis, β_1 is assumed to be fixed. Therefore, the solution $z_e = 0.002$mm can be obtained by selecting appropriate values of a_c and c_c. Obviously, if a_c and c_c are exactly equal to a and c respectively, the solution will be $z_e = 0.002$mm and the control performance is optimal. However, as mentioned before, the values of a and c are difficult to obtain because the actual model of a magnetic levitation system contains lots of uncertainties. By analyzing Eq (27), a sufficient condition for the steady-state error to be 0 is obtained. Defining $k_a = \frac{a_c}{a}$,

$k_c = \frac{0.002+c_c}{0.002+c}$, then substituting $z_e = 0.002$mm into Eq (27), a necessary condition for $z_e = 0.002$mm is obtained, it is:

$$k_a = k_c^2 \qquad (28)$$

Then, if one more condition is added, a sufficient condition for $z_e = 0.002$mm will be obtained, the sufficient condition is:

$$\begin{cases} k_a = k_c^2 \\ k_c < 1 \end{cases} \qquad (29)$$

To prove that Eq (29) is a sufficient condition for $z_e = 0.002$mm, Eq (27) is rewritten in the following form:

$$g = f_1(z_e) \cdot f_2(z_e) \qquad (30)$$

Where $f_1(z_e) = \frac{a(z_e+c_c)^2}{a_c(z_e+c)^2}$, $f_2(z_e) = g + \beta_1(z_e - 0.002mm)$. It can be known by the definitions that a, a_c, c, c_c are constantly positive and z_e is constantly non-negative. Therefore $f_1(z_e)$ is constantly positive over the domain of definition [0, $+\infty$). It is obvious that $f_2(z_e)$ is a monotonically increasing function over the domain of definition [0, $+\infty$). Since $f_1(z_e) > 0$ and $g > 0$, in order for Eq (30) to have a solution, it is necessary to make $f_2(z_e) > 0$, so both the domains of definition of $f_1(z_e)$ and $f_2(z_e)$ are adjusted to (0.002-$\frac{g}{\beta_1}$, $+\infty$). Therefore, $f_2(z_e)$ can be regarded as a monotonically increasing and constantly positive function over the domain of definition (0.002-$\frac{g}{\beta_1}$, $+\infty$). Furthermore, once $k_c < 1$ holds, $f_1(z_e)$ will also be a monotonically increasing and constantly positive function over the domain of definition [0.002-$\frac{g}{\beta_1}$, $+\infty$). In this way, $f_1(z_e) \cdot f_2(z_e)$ will also be a monotonically increasing and constantly positive function over the domain of definition [0.002-$\frac{g}{\beta_1}$, $+\infty$). Therefore, in the case where a solution exists, Eq (30) will have only one solution. That is to say, if $k_c < 1$ holds, Eq (30) will have only one solution. As mentioned before, if $k_a = k_c^2$ holds, Eq (30) will have a solution $z_e = 0.002$mm. To sum up, if $k_c > 1$ and $k_a = k_c^2$ holds simultaneously, Eq (30) will have and only have one solution, i.e., $z_e = 0.002$mm. On this basis, another control simulations were performed to verify the hypothesis shown in Fig. 13. The simulation settings are shown in Table 5. Table 5 indicates that the setting of all the group meet $k_a = k_c^2$ and $k_c < 1$, which is just proved to be a sufficient condition for the steady-state error be zero. In other words, all the simulation results will show no steady-state error. In this way, the hypothesis can be tested by observe the response of every group to F_d. If all the groups show good robustness to F_d, the hypothesis will be proven to be correct. Besides, g, d in the controller and the plant model were identical, they were 9.807m/s^2, 1.031 respectively. The simulation results are displayed in Fig. 14. If Eq (29) is met, since c and c_c are constantly positive, k_a and k_c will be limited to the intervals of (0.556, 1) and (0.3095, 1) respectively. It was proven that no matter which values in the respective intervals of k_a and k_c were taken, the simulation results were basically the same as Fig. 14(a), Fig. 14(b), Fig. 14(c) and Fig. 14(d). In other words, Fig. 14 (a), Fig. 14(b), Fig. 14(c)
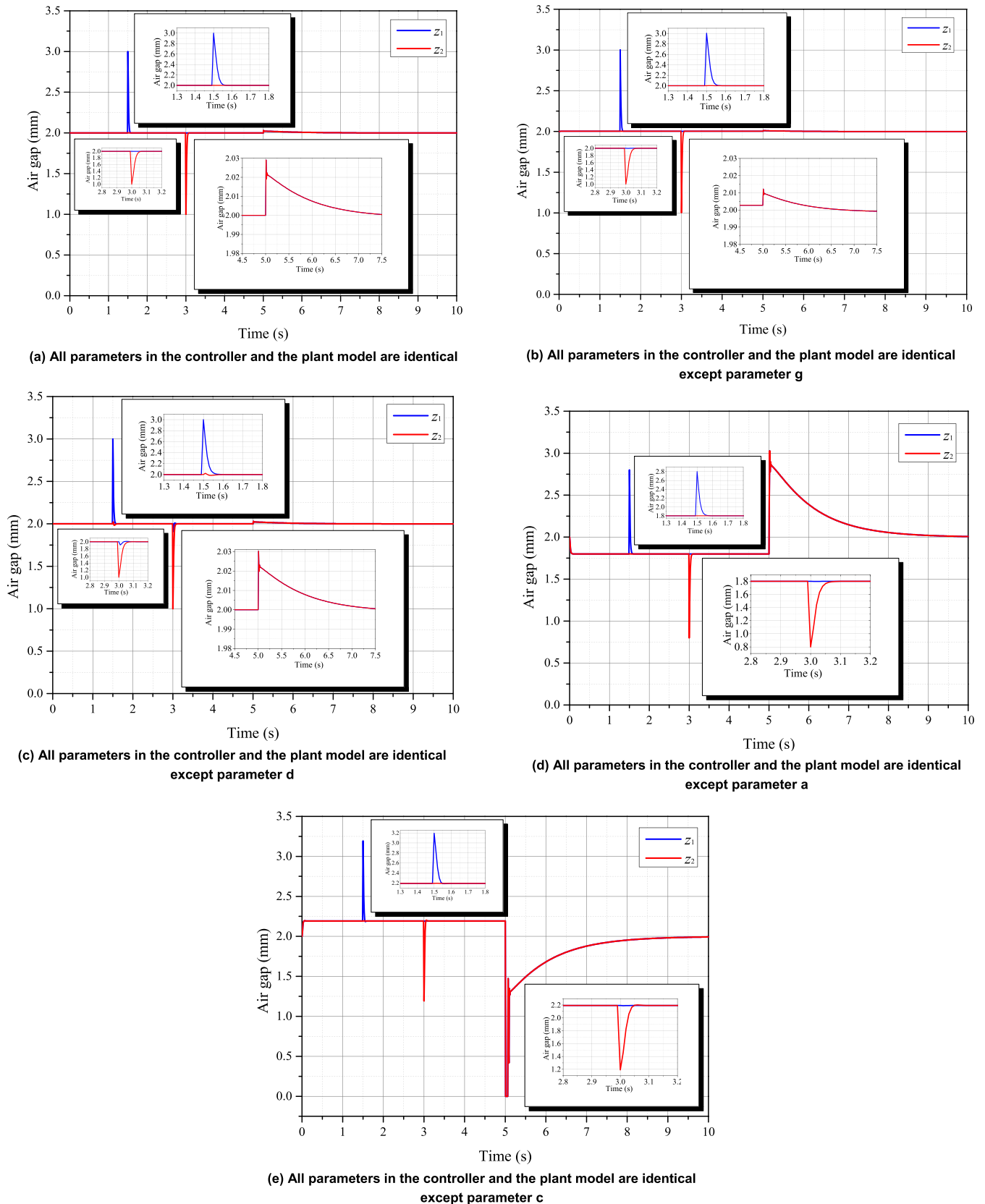
(a) All parameters in the controller and the plant model are identical

(b) All parameters in the controller and the plant model are identical except parameter g

(c) All parameters in the controller and the plant model are identical except parameter d

(d) All parameters in the controller and the plant model are identical except parameter a

(e) All parameters in the controller and the plant model are identical except parameter c

FIGURE 12. Control simulation results about the mismatch.
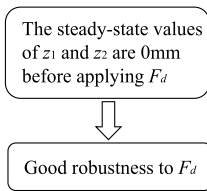
FIGURE 13. A hypothesis about the control system.

and Fig. 14(d) are the results that can represent all cases that meet Eq (29).

As shown in Fig. 14, all cases show no steady-state errors before and after applying the step disturbances. In addition, in the vicinity of 5s, all the maximum deviations are lower than 0.03mm. These results are almost identical to that of Fig. 12(a). In other words, the hypothesis shown in Fig. 13 is verified to be correct. Based on this finding, a tuning method was proposed, that is, in experiment, before applying F_d, we can set c_c to zero so that $k_c < 1$ hold, since Eq (29) is a sufficient condition for the steady-state error be zero, this means that zero steady-state error can be achieved by tuning a_c, therefore, then tune a_c make $k_a = k_c^2$ hold so that steady-state error become zero. In this way, a control system with good robustness to F_d will be obtained. To sum up, the simulation results imply that even if the accurate plant model is unknown, a good control performance can also be obtained with the proposed centralized feedback linearization as long as using the tuning method to make $k_a = k_c^2$ hold in the case of $k_c < 1$. The proposed tuning method is more convenient than making both a_c and c_c accurately match a and c respectively, because only one parameter (a_c) needs to be tuned. Furthermore, the steady-state error of the airgaps can be used as an indicator for the tuning since zero steady-state error and $k_a = k_c^2$ are sufficient and necessary conditions for each other in the case of $k_c < 1$. In Chapter VI-B and Chapter VI-C, a levitation experiment was successfully conducted with this tuning method.

V. ESTIMATION OF THE SPECIMEN ELONGATION
A. SUPPORT VECTOR MACHINE AND GRAY WOLF OPTIMIZATION
As mentioned in Chapter II-B-4) of this paper, the specimen elongation can be deduced from the bottom airgap, and ideally, the bottom airgap can be obtained by Eq (2). However, there must be a deviation between the actual model of the magnetic force and Eq (2). Therefore, support vector machine (SVM) was employed instead of Eq (2) to estimate the bottom airgap. SVM, one of machine learning methods, has good nonlinear mapping ability and doesn't rely on mathematic models, is widely used in classification and regression. In this paper, the application of SVM belongs to the regression issue. The essential idea of support vector regression is to map a nonlinear regression issue in a low-dimensional
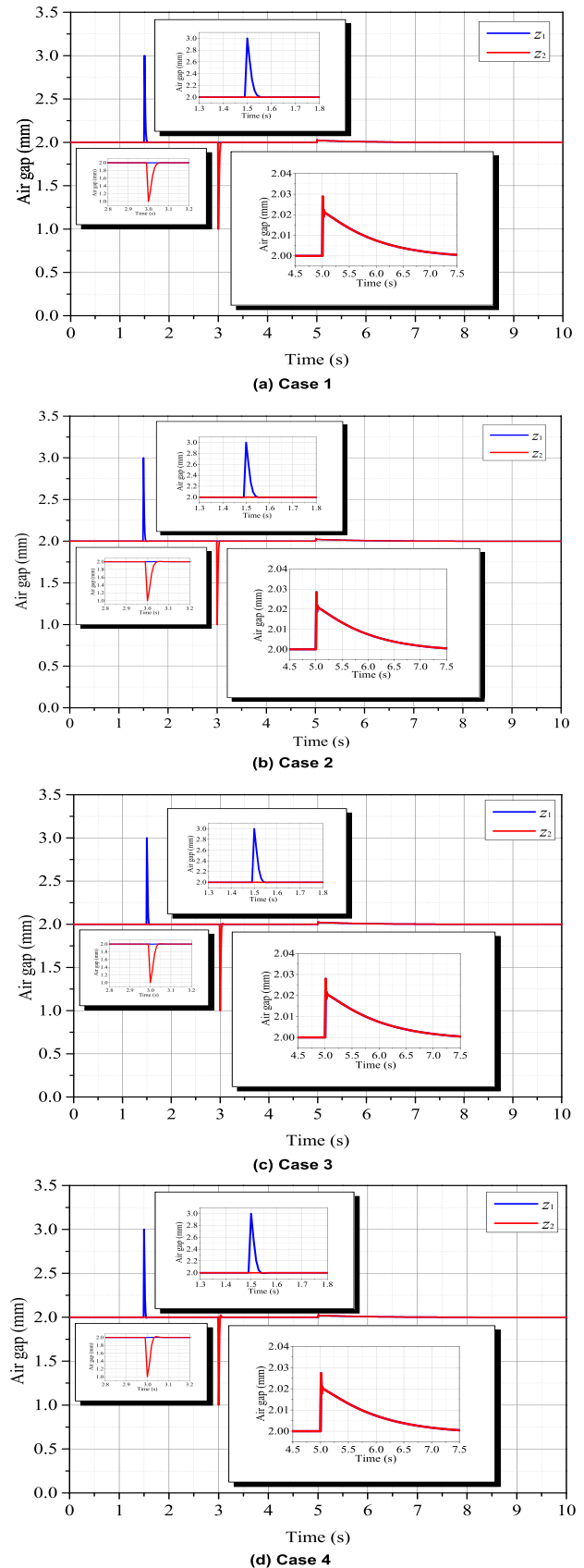

FIGURE 14. Simulation results under the conditions that $k_a = k_c^2$ and $k_c < 1$.

Simulation No.	a (Nm²A⁻²)	c (m)	a_c(Nm²A⁻²)	c_c (m)	k_a	k_c
Case 1	3.051×10^{-5}	1.595×10^{-3}	2.4713×10^{-5}	1.2355×10^{-3}	0.81	0.9
Case 2	3.051×10^{-5}	1.595×10^{-3}	1.9526×10^{-5}	0.8760×10^{-3}	0.64	0.8
Case 3	3.051×10^{-5}	1.595×10^{-3}	1.4950×10^{-5}	0.5165×10^{-3}	0.49	0.7
Case 4	3.051×10^{-5}	1.595×10^{-3}	1.0984×10^{-5}	0.1570×10^{-3}	0.36	0.6

space to a linear regression issue in a high-dimensional space by kernel function, and then solve the optimal linear regression function in the high dimensional space. For a given training set $\{(x_i, y_i), i = 1, 2, \ldots, N\}$, where $x_i \in \mathbf{R}^n$ is an N-dimensional input while $y_i \in \mathbf{R}$ is one-dimensional output. The steps of SVM to achieve regression prediction are as follows [30]:

In the high-dimensional space, the linear regression issue can be described by the following regression function:

$$f(x) = w \cdot \varphi(x) + q \qquad (31)$$

where w is a weight vector, q is a bias values, $\varphi(x)$ is a nonlinear function, which maps the nonlinearity of the sample in low-dimensional space to a linear issue in high-dimensional space. According to principle of structural risk minimization, the learning process of SVM can be stated as the following optimization issue:

$$\begin{cases} \min_{w,q,\xi_i^*,\xi_i} J = \frac{1}{2}\|w\|^2 + C \cdot \sum_{i=1}^{N}\left(\xi_i^* + \xi_i\right) \\ \text{s.t.} \begin{cases} y_i - f(x_i) \leq \varepsilon + \xi_i \\ f(x_i) - y_i \leq \varepsilon + \xi_i^* \\ \xi_i, \xi_i^* \geq 0 \end{cases} \end{cases} \qquad (32)$$

where, ξ_i^* and ξ_i are relaxation factors. ε specifies an error requirement for the regression function, a smaller ε means a smaller error in the regression function. C is a penalty factor, a larger C means a stricter penalty for samples with prediction error greater than ε. By introducing Lagrange multipliers, the optimization issue shown by Eq (32) can be converted to a dual form:

$$\begin{cases} \max_{a,a^*} \left[-\frac{1}{2}\sum_{i=1}^{N}\sum_{i=j}^{N}\left(a_i - a_i^*\right)\left(a_j - a_j^*\right)(\varphi(x_i), \varphi(x)) \right. \\ \left. -\sum_{i=1}^{N}(\alpha_i - \alpha_i^*)y_i - \sum_{i=1}^{N}(\alpha_i + \alpha_i^*)\varepsilon \right] \\ \text{s.t.} \begin{cases} \sum_{i=1}^{N}(\alpha_i - \alpha_i^*) = 0 \\ 0 \leq \alpha_i, \alpha_i^* \leq C \end{cases} \end{cases} \qquad (33)$$

where, $a = [a_1, a_2, \ldots, a_N]$ and $a^* = [a_1^*, a_2^*, \ldots, a_N^*]$ are Lagrange multipliers, $\gamma = [\gamma_1, \gamma_2, \ldots, \gamma_N]$ and $\gamma^* = [\gamma_1^*, \gamma_2^*, \ldots, \gamma_N^*]$ are loss factors. After minimizing the Lagrange function, the support vector regression issue can be formulated as follows:

$$f(x) = \sum_{i=1}^{N}\left(a_i - a_i^*\right)(\varphi(x_i), \varphi(x)) + q \qquad (34)$$

Running with kernel function $k(x_i, x)$ instead of $(\varphi(x_i), \varphi(x))$ can avoid curse of dimensionality, so Eq (34) can be rewritten as follows:

$$f(x) = \sum_{i=1}^{N}\left(a_i - a_i^*\right)k(x_i, x) + q \qquad (35)$$

There are many types of kernel function, such as polynomial kernel functions, linear kernel functions, sigmoid kernel functions and radial basis kernel functions. In this paper, the radial basis kernel function was selected:

$$K(x_i, x) = \exp\left(\frac{-\|x_i - x_j\|^2}{2\sigma^2}\right) \qquad (36)$$

where σ is the kernel width of the radial basis kernel function. Vapnik *et al.* [27]. showed that the penalty factor C determines the effect of the empirical risk generated by the training sample on the model performance, i.e., when the value of C is infinite, the SVM structural risk approaches the empirical risk; and when the value of C approaches zero, the SVM model loses prediction ability because the SVM model does not have access to the information of training sample. σ mainly affects the complexity of the distribution of the sample data in the high-dimensional feature space, because a change in the parameter σ means a change in the mapping function. To sum up, the selection of the penalty factor C and the kernel function parameter σ has a critical influence on the prediction accuracy of a SVM model. Since there is no standard guideline or method for the selection of penalty factor C and kernel function parameter σ, the selections are mostly based on experience. Therefore, in this paper, Grey wolf optimization algorithm (GWO) was employed to search for the optimal values of C and σ. The process is described as follows.

In Fig. 15(a), the data of F_3, i_3, z_3 was obtained from a simulation. These three sets of data were trained by SVM to form an estimation model with the mapping relationships of F_3, i_3, z_3. However, the model thus formed is likely to fail to achieve satisfactory estimation accuracy since the parameters C and σ are not optimized. Therefore, as shown in Fig. 15(b), with another data of F_3, i_3 and z_3, Gray wolf optimization algorithm (GWO) [30] optimized the C and σ of the estimation model based on the deviation between estimated value z_3' and real value z_3. Note that the F_3, i_3, z_3 in the

(a) Creation of estimation model

(b) Optimization of the estimation model

(c) The estimation model is involved in the work

(d) The collection of training set
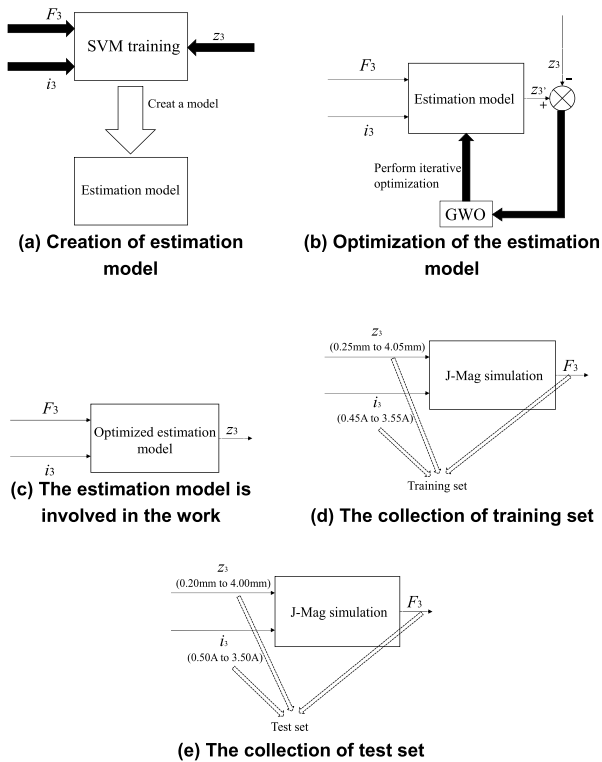
(e) The collection of test set

FIGURE 15. Estimation of the specimen elongation.

optimization process and in the creation process are not the same set, the data of F_3, i_3, z_3 in the process of creation was defined as training set while the F_3, i_3, z_3 data in the process of optimization was defined as test set. As shown in Fig. 15(d) and Fig. 15(e), both the training set and the test set were from J-Mag analysis. The selection of training set and test set is vital to the estimation model. The data chosen should be as close as possible to the actual situation. As shown in Fig. 15(d), in the training set, the i_3 varied from 0.45A to 3.55A in 0.1A step, and the z_3 varied from 0.25mm to 4.05mm in 0.1mm step. Similarly, as shown in Fig. 15(e), in the test set, the i_3 vary from 0.50A to 3.50A in 0.1A step, and the z_3 vary from 0.20mm to 4.00mm in 0.1mm step. In both sets, the F_3 was calculated by J-Mag software for all combinations of the i_3 and the z_3. These two sets of data were chosen because the ranges of the F_3 are about 0.8-50.0N and 1.0-50.0N respectively, which match the actual range of the F_3 when MLTTD works.

The GWO achieves optimization by simulating the leadership mechanism of the gray wolf population and the process of wolf tracking, encirclement, hunting, and attacking prey. In this paper, the maximum number of iterations N and the gray wolf population size T were set to 100 and 100 respectively. The steps of optimizing the estimation model with GWO were as follows [30]:

1. Initialization parameters (C = 1, σ = 1). Determine the training set and test set of the estimation model, and normalize the sample data. Set the maximum number of

iterations T of GWO and the population size N, then set the optimization both the ranges of C and σ to 100.

2. Randomly generate gray wolf group, and the individual position vector of each gray wolf group is composed of C and σ. SVM learns the training set according to the C and σ in individual positions, and calculates the fitness value of each gray wolf.

3. The gray wolf groups are classified according to fitness value, and update the individual position of each gray wolf.

4. Calculate the fitness value of each gray wolf individual at the new position and compare it with the optimal fitness value of the previous iteration, if it is better than the previous optimal fitness value, this gray wolf individual replaces the optimal fitness value of the group and let the position of this gray wolf individual replaces the previous optimal fitness value; otherwise, remain original optimal fitness value.

5. If the number of iterations exceeds the maximum number of iterations, end learning, and then output global optimal position as the optimal values of C and σ, otherwise, return to step (3) to continue parameter optimization.

6. As shown in Fig. 15(c), use optimized estimation model for prediction.

Finally, after the optimization, the optimal values of C and σ were obtained, they were 200 and 1.0541.

B. ESTIMATION RESULTS

Fig. 16 present the estimation results by the optimized estimation model. The estimation was conducted using Libsvm based on Matlab. It can be seen in Fig. 16(a) that z_3 and z_3' show good consistency in general. As shown in Fig. 16(b), the range of the estimation error is approximately −0.4 to 0.4. The root mean square error (RMSE) is 0.1353mm and the coefficient of determination (R^2) is 98.73%. In order to further analyze the estimation error, the distribution of the estimation error with z_3 was investigated. As presented in Fig. 15(c), within the airgap range of 0mm to 3.25mm, the range of the estimation error is about −0.15mm to 0.4mm. Only when z_3 is larger than 3.25mm, there are eight bad points, which are lower than −0.15mm. And as discussed in Chapter II-B-2), as long as the airgap is larger than 2.4mm, there will be enough space for the specimen to elongate. Therefore, the bottom airgap was adjusted to 3.25 mm to eliminate the bad points. The detailed steps are, the data with z_3 larger than 3.25mm in both the training set and test set were omitted to obtain new training set and test set, and then the process that depicted in Fig. 15(a), Fig. 15(b), Fig. 15(c) were implemented again with the new training set and new test set to creat a new estimation model. It is noted that this adjustment will not lead to the insufficiency of tension force and the change in magnetic characteristics of the bottom floator since the airgap was decreased rather than increased. As shown by the black points in Fig. 16(d), after adjusting the bottom airgap to 3.25mm, there are still several bad points in the top right corner. Furthermore, it was found there were always bad points even if the bottom airgap was further reduced and the estimation model was recreated in the

above manner. Therefore, it is decided that correct the new estimation model rather than recreated it. First, all the black points with z_3 larger than 3mm in Fig. 16(d) were discarded. By statistics, the average error of the remaining points is -0.09378. Then, a correction constant of 0.09378 was added to this estimation model to further reduce RMSE. In other words, the new estimation model of was completely remained except for changing the bottom airgap to 3mm and adding the correction constant. Finally, a final estimation with RMSE of 0.0843, R^2 of 98.76%, the error range of -0.1988 to 0.2269 was obtained. And the estimation error by the final estimation model is presented by the red points in Fig. 16(d).
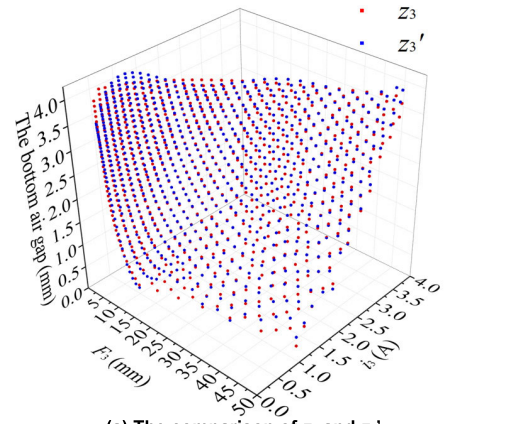
VI. EXPERIMENTS

A. EXPERIMENT SETUP

Fig. 17 present a photograph of the prototype and the overall system integration. The eddy current sensor HA-80R are made by SENTEC corporation. The power amplifier is 4-quadrant-servo amplifier ESCON 70/10, which is made by MAXON corporation. The amplifier ESCON 70/10 was set in current model, where the input 1V corresponded to 1A. The load cell 9E01-L35 is made by NEC corporation, its measuring range is ±50N. The real-time control system is based on MicroLabBox dSPACE, it is equipped with a software package Controldesk, where we can import a Simulink file, tune control parameters online and collect experiment data. The sampling frequency of the MicroLabBox dSPACE was set to 1KHz. As shown in Fig. 17(b), MicroLabBox dSPACE driver the power amplifiers by the control voltage, while sensing equipments feed the measuring data to MicroLabBox dSPACE by sensor voltage. In addition, as shown in Fig. 17(b), there were two kinds of control paths, they were levitation path and tension path. The levitation path was used to maintain the levitation of the levitated object while the tension path was used to produce tension forces at the both ends of the levitated object. In the following two kinds of experiments, i.e., levitation experiments and tension experiment, only the levitation path was enabled in the levitation experiments while both the levitation path and the tension path were enabled in the tension experiment.

B. LEVITATION EXPERIMENT SPECIFICATIONS

In order to verify the feasibility of the proposed centralized feedback linearization algorithm and the tuning method, two levitation experiments were conducted. One was by the centralized feedback linearization algorithm, the other one was by linear state feedback that proposed in paper [29] for comparison.

To ensure that the two controllers were experimented under the same conditions, all the conditions were identical except for the control parameters shown in Table 6. In particular, the filter coefficients of the differentiators in both controllers were 680 s^{-1}, which was the optimum value obtained from a large number of tentative trials. Since the tuning method

(a) The comparison of z_3 and z_3'

(b) The estimation error

(c) The distribution of the estimation error with z_3

(d) The distribution of the estimation error with z_3 after adjusting the bottom airgap to 3.25mm
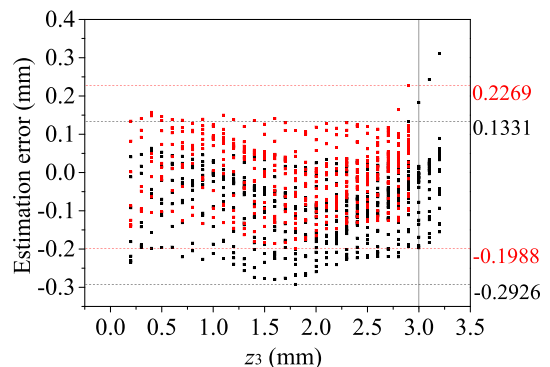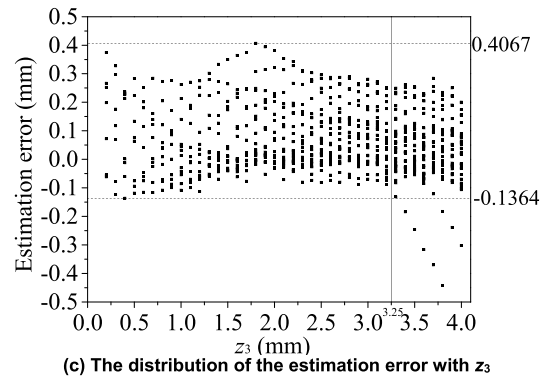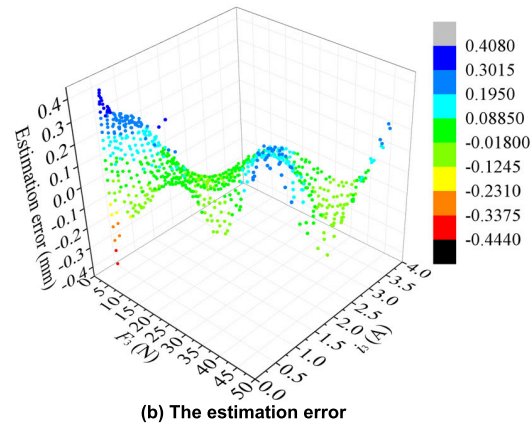
FIGURE 16. The estimation results.

(a) Photograph of the prototype

(b) Overall system structure diagram
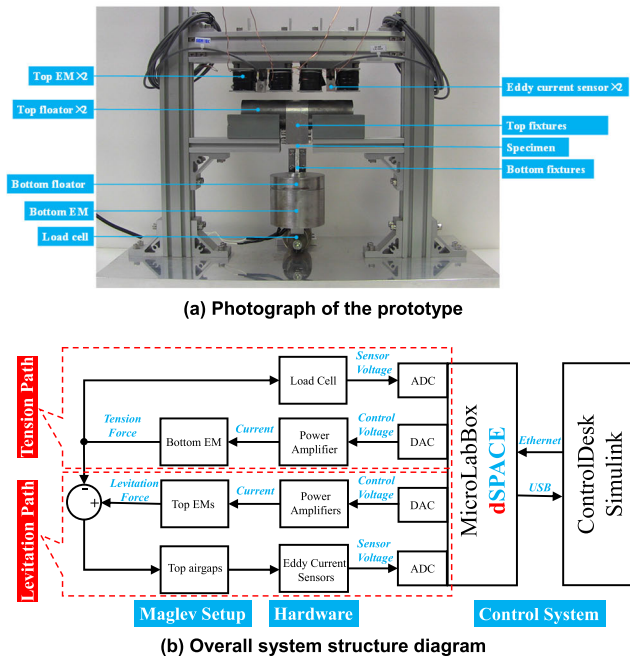
FIGURE 17. Experiment platform.

**TABLE 6.** Parameters of the controllers.

Parameters of the controllers	Linear state feedback	Centralized feedback linearization
P $(A \cdot m^{-1})$	750	No such item
D $(A \cdot s \cdot m^{-1})$	5.2	No such item
Filter coefficient of Differentiator (s^{-1})	680	680
m_1 (kg)	No such item	1.4239
g $(m \cdot s^{-2})$	No such item	9.807
d	No such item	1.08
β_1	No such item	4900
β_2	No such item	95
β_3	No such item	4900
β_4	No such item	95
a_e $(10^{-5}Nm^2A^{-2})$	No such item	2.35
c_e (m)	No such item	0

of the linear state feedback is well-known, it will not be described in this article. About the tuning method of the feedback linearization, as summarized in Chapter IV-C, set parameter c_e to zero, and then tune parameter a_e with steady-state error of the airgaps as indicators to meet Eq (28). Therefore, in this experiment, parameter c_e was fixed to 0mm. And a_e, β_1, β_2, β_3 and β_4 were firstly set to 3.051×10^{-5}N·m^{2}A^{-2}, $9800\,s^{-2}$, $180\,s^{-1}$, $9800\,s^{-2}$, $180\,s^{-1}$ respectively, which were obtained from simulation. Subsequently, according to the magnitude of the magnetic force generated, only parameter a_e was tuned to enable levitation. In more detail, when the magnetic force was too large, tune parameter a_e upwards, and vice versa, until the levitated objects were successfully levitated. After successful levitation, if the steady-state errors of the airgaps were positive, parameter a_e
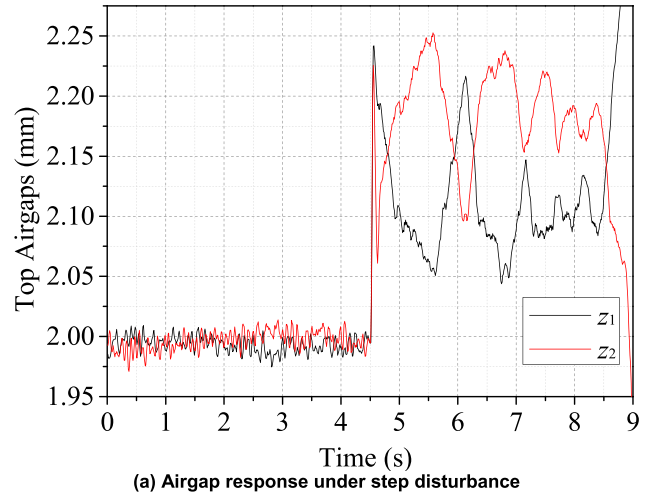
(a) Airgap response under step disturbance
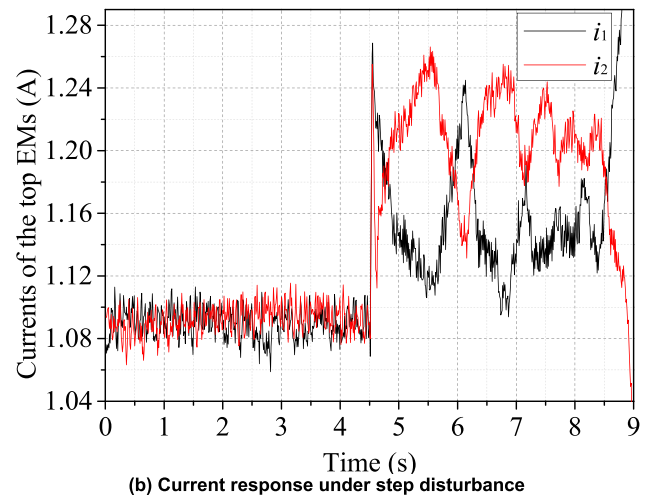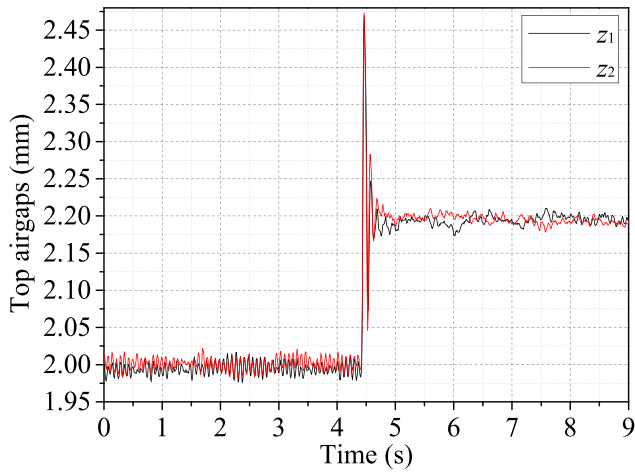

(b) Current response under step disturbance

FIGURE 18. Experiment results by the linear state feedback.

should be tuned downwards, and β_1, β_2, β_3, β_4 should also be reduced appropriately to eliminate vibration. In contrast, if the steady-state errors of the airgaps were negative, parameter a_e should be tuned upwards, and β_1, β_2, β_3, β_4 should also be increased appropriately to provide sufficient magnetic force. In this way, the parameters were continuously tuned until the steady-state errors became 0mm. the finalized values of the parameters were shown in Table 6.
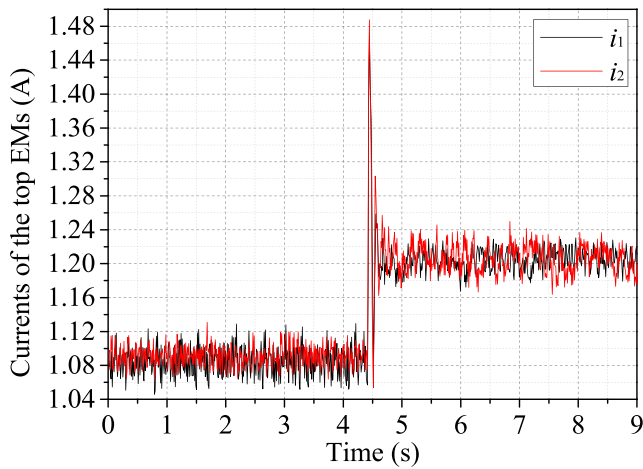
C. LEVITATION EXPERIMENT RESULTS

Fig. 18 and Fig. 19 give the experiment results. As shown in Fig. 18 and Fig. 19, in both experiments, levitations started at 0s, and two step disturbances were applied at around 4.5s. It is noted that the magnitudes of the two step disturbances were not the same. The two step disturbances are the maximum disturbances that the two systems can withstand, respectively. They are 0.15mm and 0.20mm respectively. In addition, in order to ensure the rigor of the experiments, both the two maximum step disturbances were obtained by extensive trials with different parameters of their respective controllers. They

(a) Airgap response under step disturbance

(b) Current response under step disturbance

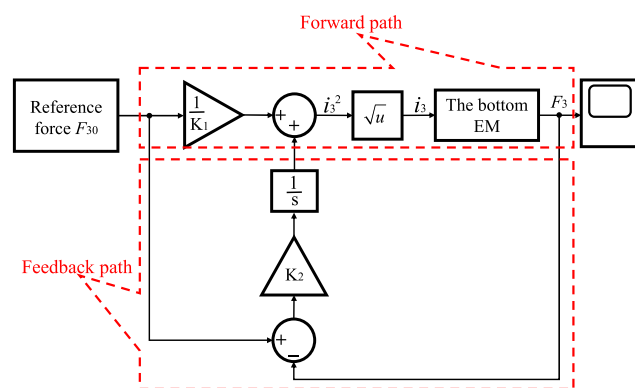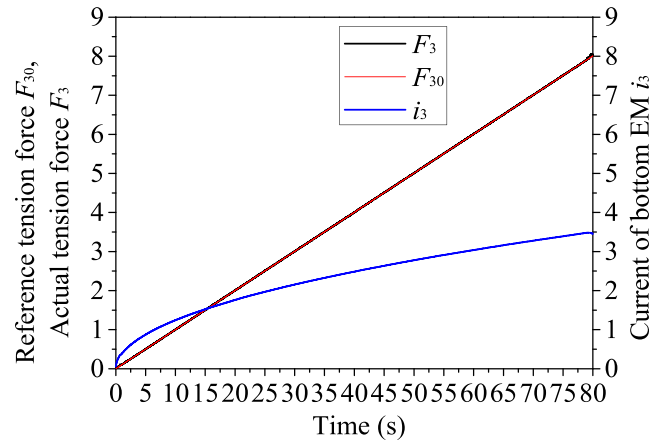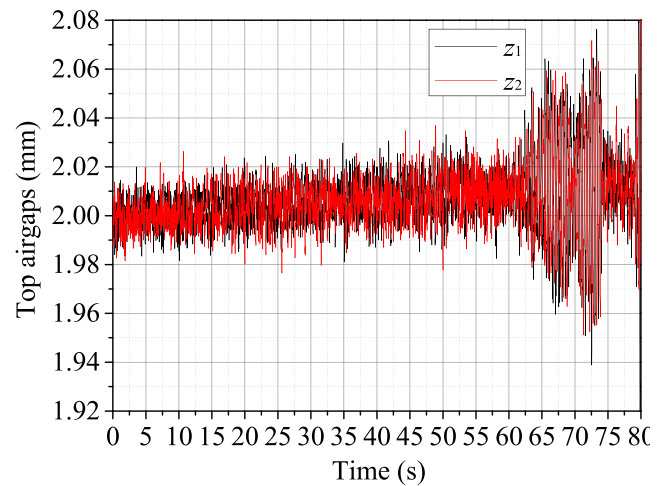**FIGURE 19.** Experiment results by the centralized feedback linearization.

FIGURE 20. Control of the tension force F_3.

(a) Control results of the tension force

(b) Airgap response under the tension force

(c) Current response under the tension force
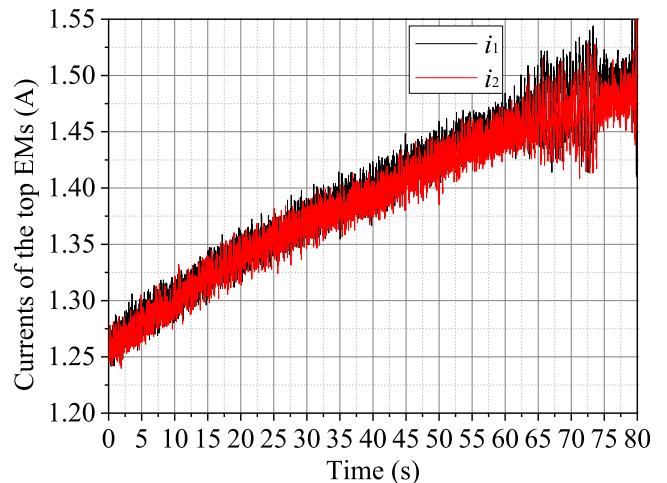
FIGURE 21. Tension experiment results.

reflect the best performance of their respective controllers. In other words, the results presented in Fig. 18 and Fig. 19 are not an accidental result caused by the control parameters not being tuned well. It can be seen in Fig. 18, after applying the

0.15mm step disturbance, with the alternating rise and fall of the two airgaps, the levitation only lasted for about 4.5s before it ended. In contrast, as shown in Fig. 19, the levitation remained stable even with the 0.2mm step disturbance applied. This implies the centralized feedback linearization controller has stronger robustness than the linear state feedback controller.

TABLE 7. Definition of abbreviations over this article.

Abbreviation	Definition
DoF	Degree of freedom
EM	Electromagnet
SVM	Support vector machine
RMSE	Root mean square error
R^2	Coefficient of determination
SEM	Scanning electron microscope
Maglev	Magnetic levitation
MLTTD	The magnetic levitation tension testing device
GWO	Gray wolf optimization

D. TENSION EXPERIMENT SPECIFICATIONS

On the basis of levitation experiment, tension experiments were conducted with the centralized feedback linearization control algorithm. Due to the addition of the bottom floator and bottom fixtures, Some of the control parameters were adjusted, they were $m_1 = 1.9307$kg, $\beta_1 = \beta_3 = 4000$ s^{-2}, $\beta_2 = \beta_4 = 85$ s^{-1}, $a_e = 2.46 \times 10^{-5}$Nm^{2}A^{-2}, d = 1.13. The rest control parameters remained the same as Table 6. In addition, to control the tension force (F_3), as shown in Fig. 20, a control system was proposed. This control system was proposed based on Eq (37), where a_3 and c_3 are two constants, z_3 is the bottom airgap. As shown in Eq (37), ignoring the impact of change in z_3, it can be assumed that F_3 be equal to K$_1 \cdot i_3$, where K$_1$ is a constant. On this basis, the forward path in Fig. 20 was proposed. In addition, the feedback path in Fig. 20 was employed to compensate for the deviation caused by changes in z_3. In the experiment, the values of K$_1$ and K$_2$ were 0.588 and 13 respectively. With such a control system, the tension force was gradually applied at a rate of 0.1N/s to the bottom EM. Fig. 21(a) presents the actual tension force F_3 measured by the load cell and the reference tension force F_{30}.

$$F_3 = \frac{a_3}{(z_3 + c_3)^2} \cdot i_3^2 \approx K_1 \cdot i_3^2 \qquad (37)$$

E. TENSION EXPERIMENT RESULTS

Fig. 21(a) gives the control result of the tension force F_3 while Fig. 21(b) and Fig. 21(c) give the airgap response and current response respectively. As shown in Fig. 21(b), although the airgaps slightly rose in the first 60s, the increments were less than 0.02mm, meanwhile, as shown in Fig. 21(c), the currents of the top EMs gradually increased to compensate for the tension force. In addition, from 60s to 80s, the amplitudes of the airgaps became much larger than before. Nevertheless, as can be seen in Fig. 21(a), between 60s and 80s, there was almost no impact on the proceeding of the tension force F_3 even though the amplitudes of airgaps became larger, which validate the effectiveness of the control system shown in Fig. 20. To sum up, it can be concluded that the whole control system copes well with the tension force. Up to now, the maximum value of F_3 that the device can withstand is 8.05N, and the floator and fixtures weigh 4.97N, totally, the device applied a 13.02N tension force to the specimen. In other words, the developed testing device and the proposed control system are feasible within a certain force range.

VII. CONCLUSION

In this paper, a maglev tension testing device where a specimen can be tested while it is levitated was developed. To guarantee the alignment of the tension force, the magnetic characteristics of three shapes of floators were investigated via electromagnetic analysis. It was found that a ring floator combine the advantages of strong magnetic force, low mass, and easy alignment of the tension force. Also, the structure of the device was minimized while ensuring sufficient magnetic force. In addition, a centralized feedback linearization control algorithm was proposed for the device. Furthermore, control simulations demonstrated that the proposed feedback linearization control algorithm has satisfactory dynamic performance and robustness even in the case of a mismatch between the controller and the plant. Moreover, an SVM-based model for estimating specimen elongation was established. After iterative optimization and correction, the final estimation model performed with the estimation error range of -0.1988mm to 0.2269mm, RMSE of 0.0843mm and R^2 of 98.76%. Finally, a levitation experiment and a tension experiment are given to prove the feasibility of MLTTD. Levitation experiment results demonstrated that the proposed feedback linearization control algorithm is convenient to tune and has stronger robustness than the linear control algorithm. The tension experiment results indicated the prototype can withstand a tension force up to 13.02N.

Up to now, the maximum tension force that the device can withstand is 13.02N. We speculate that the reason of the limit may be due to the displacement sensor noise becoming larger as the top EMs current increases. Because the two displacement sensors are eddy current sensors, they are susceptible to magnetic interference, and they are close to the top EMs. We will do further research on it, and make MLTTD to withstand larger tension force.

REFERENCES

[1] T. Akitsu, K. Kajiwara, K. Tachiiri, H. Kobayashi, K. Matsumoto, T. Kobayashi, K. N. Nasahara, T. Nakaji, H. Kobayashi, T. Okano, N. Saigusa, M. Hayashi, R. Ide, and Y. Honda, "Validating GCOM-C terrestrial ecology products: How should *in-situ* observation be performed at satellite scale?" in *Proc. IGARSS*, Yokohama, Japan, Jul. 2019, pp. 9196–9199.

[2] Z. Islam, M. Xian, A. Haque, F. Ren, M. Tadjer, N. Glavin, and S. Pearton, "*In situ* observation of β-Ga$_2$O$_3$ Schottky diode failure under forward biasing condition," *IEEE Trans. Electron Devices*, vol. 67, no. 8, pp. 3056–3061, Aug. 2020.

[3] S. Li, "Design analysis and experimental research of in-situ torsion testing equipment for mechanical properties of materials," Ph.D. dissertation, Dept. Mech. Eng., Jilin Univ., Jilin, China, 2015.

[4] S. Comby-Dassonneville, F. Charlot, R. Martin, F. Roussel-Dherbey, L. Maniguet, D. Pellerin, F. Volpi, C. Boujrouf, G. Parry, M. Braccini, S. Iruela, A. Antoni-Zdziobeka, Y. Champion, and M. Verdier, "Development and application of a multifunctional nanoindenter: Coupling to electrical measurements and integration *in-situ* in a scanning electron microscope," in *Proc. HOLM*, Milwaukee, WI, USA, Sep. 2019, pp. 1–8.

[5] M. Sikul, K. Novotny, M. Kemmler, and A. Rummel, "SEM-based nanoprobing on *in-situ* delayered advanced 10 nm technology node IC," in *Proc. IPFA*, Singapore, Jul. 2018, pp. 1–4.

[6] A. Christou, F. Liu, and R. Dahiya, "Assessing the stability of printed NWs by *in situ* SEM characterisation," in *Proc. FLEPS*, Manchester, U.K., Aug. 2020, pp. 1–4.

[7] P. Wang, H. Lu, and Y. Shen, "Flexible 3-D helix fabrication by *in-situ* SEM micromanipulation system," *IEEE Trans. Ind. Electron.*, vol. 67, no. 7, pp. 5565–5574, Jul. 2020.

[8] N. Tada and T. Uemori, "Time-dependent fracture of copper-cored lead-free solder ball and nickel rod joints in air, distilled water, and NaCl solution," in *Proc. IMPACT*, Taipei, Taiwan, Oct. 2017, pp. 168–171.

[9] N. Tada and H. Masago, "Evaluation of tensile strength of copper-cored lead-free solder joints in air, distilled water, and NaCl solution using testing device with permanent magnets," in *Proc. IMPACT*, Taipei, Taiwan, Oct. 2014, pp. 92–95.

[10] N. Hasegawa, S. Sakuma, Y. Murozaki, and F. Arai, "Mechanical characterization of ultra-thin membrane using force sensing chip," in *Proc. MHS*, Nagoya, Japan, Dec. 2017, pp. 1–3.

[11] M. He, S. Chen, W. Xia, and B. Wang, "Nano-mechanical properties of Sn micro-bumps," in *Proc. ICEPT*, Changsha, China, Aug. 2015, pp. 1054–1057.

[12] S. Sakuma, Y. Gao, Y. Murozaki, and F. Arai, "Tensile characterization of thin biomembrane," in *Proc. TRANSDUCERS EUROSENSORS XXXIII*, Berlin, Germany, Jun. 2019, pp. 417–420.

[13] N. Tada, R. Nishihara, and H. Masago, "Tensile test of small lead-free solder joint using permanent magnet," in *Proc. IMPACT*, Taipei, Taiwan, Oct. 2012, pp. 145–148.

[14] N. Tada and H. Masago, "Remotely-controlled tensile test of copper-cored lead-free solder joint in liquid using permanent magnet," in *Proc. IMPACT*, Taipei, Taiwan, Oct. 2013, pp. 186–189.

[15] A. M. Benomair and M. O. Tokhi, "Control of single axis magnetic levitation system using fuzzy logic control," in *Proc. SAI*, London, U.K., Jul. 2015, pp. 514–518.

[16] I. Iswanto and A. Ma'arif, "Robust integral state feedback using coefficient diagram in magnetic levitation system," *IEEE Access*, vol. 8, pp. 57003–57011, 2020.

[17] A. Mughees and S. A. Mohsin, "Design and control of magnetic levitation system by optimizing fractional order PID controller using ant colony optimization algorithm," *IEEE Access*, vol. 8, pp. 116704–116723, 2020.

[18] Y. Sun, J. Xu, G. Lin, W. Ji, and L. Wang, "RBF neural network-based supervisor control for maglev vehicles on an elastic track with network time delay," *IEEE Trans. Ind. Informat.*, vol. 18, no. 1, pp. 509–519, Jan. 2022.

[19] Y. Sun, J. Xu, H. Wu, G. Lin, and S. Mumtaz, "Deep learning based semi-supervised control for vertical security of maglev vehicle with guaranteed bounded airgap," *IEEE Trans. Intell. Transp. Syst.*, vol. 22, no. 7, pp. 4431–4442, Jul. 2021.

[20] R.-J. Wai, J.-X. Yao, and J.-D. Lee, "Backstepping fuzzy-neural-network control design for hybrid maglev transportation system," *IEEE Trans. Neural Netw. Learn. Syst.*, vol. 26, no. 2, pp. 302–317, Feb. 2015.

[21] D. L. Trumper, S. M. Olson, and P. K. Subrahmanyan, "Linearizing control of magnetic suspension systems," *IEEE Trans. Control Syst. Technol.*, vol. 5, no. 4, pp. 427–438, Jul. 1997.

[22] R. Uswarman, A. I. Cahyadi, and O. Wahyunggoro, "Control of a magnetic levitation system using feedback linearization," in *Proc. IC3INA*, Jakarta, Indonesia, Nov. 2013, pp. 95–98.

[23] B. Tandon, S. Kaur, and A. Kalra, "Stability analysis of feedback linearized magnetic levitation system using sum-of-squares method," in *Proc. ISPCC*, Solan, India, Sep. 2017, pp. 420–424.

[24] A. M. Benomair, F. A. Bashir, and M. O. Tokhi, "Optimal control based LQR-feedback linearisation for magnetic levitation using improved spiral dynamic algorithm," in *Proc. MMAR*, Miedzyzdroje, Poland, Aug. 2015, pp. 558–562.

[25] S. K. Pradhan and B. Subudhi, "Nonlinear control of a magnetic levitation system using a new input-output feedback linearization," in *Proc. IFAC*, Tiruchirappalli, India, 2016, pp. 1–5.

[26] Q. Chen, Y. Tan, Q. Yang, J. Li, and I. Mareels, "Centralized control implementation using distributed observer for Meglev systems," in *Proc. CCC*, Dalian, China, Jul. 2017, pp. 9966–9971.

[27] O. Chapelle, V. Vapnik, O. Bousquet, and S. Mukherjee, "Choosing multiple parameters for support vector machines," *Mach. Learn.*, vol. 46, no. 1, pp. 131–159, Feb. 2002.

[28] H. Kwakernaak and R. Sivan, *Linear Optimal Control Systems*. New York, NY, USA: Wiley, 1972, pp. 193–319.

[29] M. Ren and K. Oka, "Design and analysis of a magnetic levitation tension testing device," in *Proc. IECON*, Toronto, ON, Canada, Oct. 2021, pp. 1–7.

[30] Z. Yang, Y. Wang, and C. Kong, "Remaining useful life prediction of lithium-ion batteries based on a mixture of ensemble empirical mode decomposition and GWO-SVR model," *IEEE Trans. Instrum. Meas.*, vol. 70, pp. 1–11, 2021.

MENGYI REN (Graduate Student Member, IEEE) received the M.E. degree in mechanical engineering from Jiangnan University, Wuxi, China, in 2020. He is currently pursuing the Ph.D. degree with the Department of Intelligent Mechanical Systems Engineering, Kochi University of Technology.

His research interests include design and application of magnetic levitation and nonlinear control of magnetic levitation.

KOICHI OKA (Member, IEEE) received the M.E. degree in mechanical engineering from Kyoto University, Kyoto, Japan, in 1983, and the Ph.D. degree in mechanical engineering from The University of Tokyo, Tokyo, Japan, in 1997.

From 1985 to 1992, he was a Research Associate with the Institute of Industrial Science, The University of Tokyo, where he was a Research Associate with the Faculty of Engineering, from 1992 to 1999. He is currently a Professor with the Department of Intelligent Mechanical Systems Engineering, Kochi University of Technology, Kochi, Japan. He has authored or coauthored more than 60 technical papers and two books. His research interests include magnetic levitation systems, bearingless motor, and robotics.

● ● ●